U C • FCTUC FACULDADE DE CIÊNCIAS E TECNOLOGIA UNIVERSIDADE DE COIMBRA

André José Ferreira Gorgulho

Image-Derived Input Function for Brain PET Quantification

Dissertação apresentada à Universidade de Coimbra
para cumprimento dos requisitos necessários à
obtenção do grau de Mestre em Engenharia Biomédica.

Orientador: Doutor Miguel Patrício (Faculdade de Medicina da Universidade de Coimbra)

Coimbra, Fevereiro de 2015

Este trabalho foi desenvolvido em colaboração com:

ICNAS

Instituto de Ciências

Nucleares

Aplicadas à Saúde

Agradecimentos

Em primeiro lugar, quero agradecer ao orientador da minha tese, o Doutor Miguel Patrício. Obrigado por todo o apoio prestado ao longo deste projecto, pela confiança depositada no meu trabalho, por se preocupar com o meu sucesso e por todos os conhecimentos que me transmitiu. Tive ajuda sempre que precisei, com atenção dada ao pormenor, e por isso estou muito grato. Agradeço também ao Doutor Francisco Caramelo pelo tempo disponibilizado para esclarecimento de dúvidas.

Quero agradecer também ao Prof. Doutor Miguel Morgado pelo seu trabalho na coordenação do curso de Mestrado Integrado em Engenharia Biomédica, que desempenhou um papel fundamental na criação de oportunidades e tomada de decisões ao longo do meu percurso universitário.

Este projecto marca a conclusão de mais uma etapa. E como em todas as outras na vida, sinto-me feliz e agradecido por poder contar com o apoio incondicional da minha família e amigos. Em especial, quero agradecer aos meus pais e avós pela confiança, motivação e amor e por todo o apoio essencial para a concretização dos meus objectivos. Obrigado.

Resumo

A técnica de imagiologia de tomografia por emissão de positrões (PET, acrónimo inglês de Positron Emission Tomography) permite medir a concentração de radiofármaco e visualizar a sua distribuição espacial e temporal. Porém, é possível obter informação quantitativa mais específica a nível da cinética do radiofármaco utilizado no exame. Foram desenvolvidos métodos matemáticos que permitem isolar o sinal correspondente à concentração de radiofármaco que interage com a molécula-alvo para que foi previamente desenhado. O estudo da cinética de moléculas relevantes contribui significativamente para desvendar mecanismos moleculares responsáveis por doenças.

O ponto de partida para uma análise quantitiva de imagens PET é frequentemente um modelo compartimental. Neste modelo, em cada *voxel* é assumido que existem aglomerações homogéneas de radiofármaco e que cada aglomeração pode ser representada como um compartimento. Cada compartimento é associado a um possível estado do radiofármaco, referindo-se à interacção com a molécula alvo, interacção com outras moléculas não relevantes, sem qualquer interação ou estando presente nos vasos sanguíneos, nomeadamente no plasma. Considera-se que o radiofármaco pode alternar entre compartimentos, e tipicamente assume-se ainda que a variação da concentração de um compartimento se encontra linearmente relacionada com a concentração de radiofármaco nos outros compartimentos. O que se pretende determinar são as constantes de linearidade que relacionam as concentrações nos vários compartimentos, e que irão descrever a cinética do radiofármaco.

Para calcular as contantes cinéticas, é necessário determinar uma função de *input* para o modelo, que corresponde à evolução da concentração de radiofármaco no plasma com o tempo. O método *gold-standard* para obter esta função consiste na amostragem de sangue arterial feita ao longo do exame PET, através da canulação da artéria radial. Porém, este apresenta várias desvantagens. É invasivo, desencoraja voluntários saudáveis e pacientes de participar em estudos clínicos e, para além de laborioso, inclui um risco de exposição à radiação. Outro ponto a considerar é que a função determinada deste modo tem de ser calibrada em relação aos dados PET e corrigida para um factor de atraso, tendo em conta que a medição da concentração de radiofármaco é feita no braço, e geralmente a zona em estudo é o cérebro.

Entre outras alternativas que foram desenvolvidas como possíveis substitutas da canulação da artéria radial, uma técnica interessante é a derivação da função de *input* directamente das imagens PET. Pretende-se deste modo obter uma função de input derivada da imagem (IDIF, acrónimo inglês para Image-Derived Input Function). A determinação de IDIFs para estudos cerebrais pode ser conseguida através da definição de volumes de interesse (VOI, acrónimo inglês para Volume of Interest) nas imagens PET, nas zonas correspondentes às artérias carótidas internas. Este método tem potencial para constituir uma alternativa não invasiva e já foi implementado com sucesso para alguns radiofármacos.

O presente trabalho tem como objectivo investigar métodos para estimar IDIFs no contexto do trabalho desenvolvido no IBILI/ICNAS. Após uma revisão do estado da arte do problema, foi feito um estudo usando um fantoma computacional. Posteriormente, métodos para estimar IDIF foram aplicados a imagens PET de [^{11}C]-Raclopride para determinar a função de *input* arterial e efectuar a quantificação das correspondentes imagens PET. Os resultados da quantificação foram comparados com resultados obtidos utilizando uma técnica de quantificação já validada para [^{11}C]-Raclopride.

Abstract

The Positron Emission Tomography (PET) imaging technique allows the measurement of radioligand concentration in the scanned regions and consequently a visualization of its spatial and temporal distribution. Nevertheless, more precise information about its kinetics is often sought. Mathematical quantification methods allow isolating the signal corresponding to the concentration of radioligand bonded to its predefined specific molecular target. A more precise understanding of the kinetics of relevant molecules significantly contributes to unveiling mechanisms responsible for diseases or malfunctions.

The starting point for the quantification analysis of PET images is often a compartmental model. In each voxel it is assumed that there are homogeneous pools of radioligand and each pool is represented as a compartment. Each compartment is associated to a possible condition of the radioligand, as being specifically bound to the target molecule, bound to other non relevant molecules, free or circulating in vessels. It is considered that the radioligand can exchange between compartments and that the concentration change of radioligand in one compartment is a linear function of the concentration of radioligand in the other compartments. One seeks to determine the constants that relate the compartments, which describe the kinetics of the radioligand.

Calculating the parameters of interest requires the determination of the arterial plasma input function (AIF), which is the time-varying plasma concentration of radiotracer, and is the input for the model. The gold-standard method for obtaining AIF is measuring the radioactivity of arterial blood samples, which relies on the cannulation of the radial artery. However, this procedure has several disadvantages. It is invasive, it discourages healthy volunteers and patients from participating in clinical research and may be considered laborious for the research personnel. Another point to consider is that the function extracted with this technique has to be calibrated according to the PET data and corrected for a delay factor, resulting from the time that the radiotracer takes to travel from the arm, where the blood samples are taken from, to the brain, which is frequently the region in which one is interested to study.

Among some alternatives to arterial sampling, an attractive one is deriving the input function from the image data, thus obtaining an image-derived input function (IDIF). IDIFs for brain PET studies are typically extracted by measuring the radioligand

concentration from a defined volume of interest (VOI) placed in the region matching the internal carotid arteries. This technique has the potential to constitute a non-invasive alternative to arterial cannulation as has been successfully applied for some radiotracers.

In this study we look at different IDIF methods described in the literature and develop some alternatives. The latter are compared to a well-established method using a computational phantom. IDIF methods are also applied to [^{11}C]-Raclopride PET data to estimate the arterial input function and further calculate quantification parameters. The quantification estimates derived using IDIF are compared to those obtained using an alternative validated quantification method for [^{11}C]-Raclopride PET.

List of Abbreviations

AIF	Arterial Input Function
BP	Binding Potential
DV	Distribution Volume
DVR	Distribution Volume Ratio
EM	Expectation Maximization
FDG	Fluor-Deoxy-Glucose
H4V	Hottest Four Voxels
HC	Hybrid Chen
HPLC	High-Performance Liquid Chromatography
HRRT	High-Resolution Research Tomograph
ICA	Independent Component Analysis
IDIF	Image-Derived Input Function
MR	Magnetic Resonance
MRI	Magnetic Resonance Imaging
PET	Positron Emission Tomography
PVE	Partial Volume Effects
PBIF	Population-Based Input Function
RBC	Red Blood Cells
ROI	Region of Interest
RTM	Reference Tissue Model
SIME	Simultaneous Estimation
SRTM	Simplified Reference Tissue Model
TAC	Time-Activity Curve
VOI	Volume of Interest

List of Figures

List of Tables

Table of Contents

1. Introduction

1.1. Brain-PET Quantification and the Input Function

Positron emission tomography (PET) images enable the visualization of a radiotracer's distribution as a function of time, but often more specific quantification of its kinetics is sought. After the data has been reconstructed, further mathematical quantification methods allow isolating the signal corresponding to the concentration of radiotracer bound to its predefined specific target. The underlying notion is that PET allows the measurement of tracer concentration in the scanned regions, not discriminating between specific binding, non-specific binding, free tracer or tracer in plasma. More precisely, understanding the kinetics of relevant molecules allows unveiling target mechanisms responsible for diseases or malfunctions.

The starting point for the quantification analysis of PET images is often a compartmental model. This model assumes that there are physiological homogeneous pools of radiotracer. Each pool is represented as a compartment, see figure 1.1. Various techniques have been proposed to quantify receptor kinetics using compartmental models, with varying model and experimental designs, invasiveness and mathematical solution (Watabe et al. 2006). Compartmental models are expressed by an initial boundary value problem that relates the concentrations of radiotracer in the different compartments and where the coefficients are the kinetic parameters.

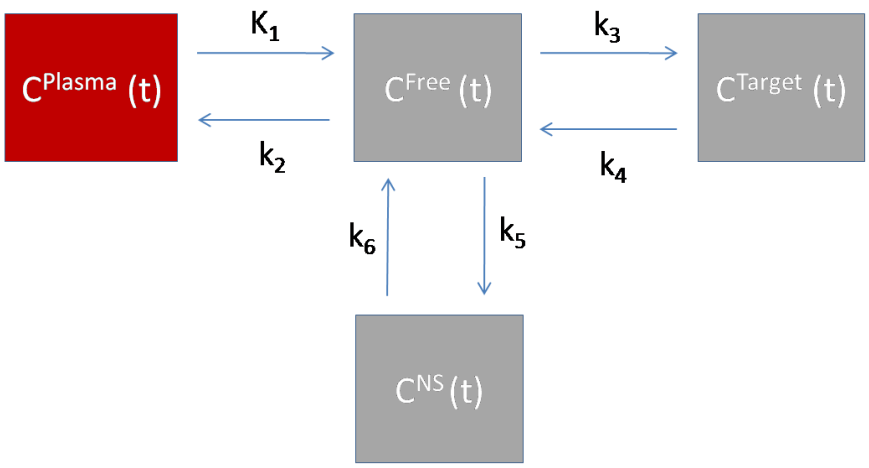

Figure 1.1 – General three-tissue compartmental model. Here the flow of concentration of radiotracer between 4 compartments (plasma concentration C^{Plasma} , free compartment C^{Free}, specific binding to a target molecule C^{Target} and non-specific bindingC^{NS}) is illustrated. The tracer concentration given by the PET image is a summation of C^{Free}, C^{Target} and C^{NS}.

Several different compartmental models have been proposed. Typically the concentration differences between two compartments are assumed to be linearly related to the transport and binding rates of the tracer. Considering the 4 compartments illustrated in figure 1.1, the model reads:

$$\frac{dC^{Target}(t)}{dt} = k_3 C^{Free}(t) - k_4 C^{Target}(t) \quad (1.1)$$

$$\frac{dC^{NS}(t)}{dt} = = K_1 C^{Plasma}(t) + k_6 C^{NS}(t) + k_4 C^{Target}(t) - (k_2 + k_3 + k_5) C^{Free}(t) \quad (1.2)$$

$$\frac{dC^{NS}(t)}{dt} = k_5 C^{Free}(t) - k_6 C^{NS}(t) \quad (1.3)$$

where K_1, k_2, k_3, k_4, k_5 and k_6 are the transfer rate constants. These are the parameters of interest that one is interested in obtaining from equations 1.1 to 1.3. In this process, often more precision is obtained by combining rate constants. Deriving macro parameters, which are combinations of the transfer rate constants, such as the distribution volume (DV) or the binding potential (BP) is also in many cases more meaningful for data analysis.

Determining the parameters of interest requires more information to be collected besides the PET data. It requires the estimation of the arterial plasma concentration of tracer in time, which is the input function for the model. The gold-standard method for obtaining this arterial input function (AIF) is arterial sampling. In this process, during the PET exam, typically the cannulation of the radial artery is made to collect several arterial blood samples and for each the radioactivity in plasma is measured. However, this procedure has several disadvantages. It is invasive, though rarely dangerous (Everett et al. 2009), it discourages healthy volunteers and patients from participating in clinical research and may be considered laborious for the research personnel (Zanotti-Fregonara et al. 2011). Another point to consider is that the samples are taken from the arm, and the radiotracer concentration in plasma is sought on the brain area. Ideally, the plasma time-activity curve (TAC) should be measured as near as possible to the brain.

To avoid the invasiveness of the arterial cannulation, some less invasive or totally non-invasive alternatives were developed. Population-based input function (PBIF) consists on using a standard input function obtained from a population of subjects, scaled using some blood samples or individual noninvasive parameters. However this method has some limitations, since the shape of the input function may be very specific for an individual according to variations in the metabolism of the radioligand. A totally non-invasive alternative to arterial cannulation is given by extending compartmental models to include a reference tissue where it is assumed that specific binding does not occur. However, these reference region analysis are only applicable if that assumption indeed holds, which must be carefully evaluated and is not always case for all diseases (Kropholler et al. 2007) nor for all the radiotracers used. Moreover, they may result in loss of accuracy and increased bias (Liptrot et al. 2004).

In this thesis, we will focus on a different alternative, Image-derived Input Function (IDIF) method.

1.2. Image-derived Input Function – Idea, Advantages/Disadvantages and Obstacles

In order to overcome the limitations associated to the gold-standard method for obtaining the AIF, it was proposed that the input function would be taken directly from PET images. The idea of using an IDIF for brain PET quantification is a very attractive

solution. Ideally it allows to locally compute the input function non-invasively, avoiding calibration and radioactivity measurement errors associated with arterial sampling.

A downside of the IDIF method is that it requires access to large blood pools. It has been validated for some applications using the heart (Choi et al. 1991) or the femoral arteries (Lüdemann et al. 2006). In brain studies, where there are no large blood pools in the field of view, the IDIF has to be estimated from intracranial blood vessels, usually the internal carotid arteries, which deliver the radiotracer to the brain. Unlike the heart or the femoral arteries, carotid arteries are small, their diameter averaging 5 mm, whereas the spatial resolution of modern PET cameras is often about 6 mm (Zanotti-Fregonara et al. 2011). This constitutes a major obstacle since partial volume effects (PVE), spill-in and spill-out, strongly influence the results. Spill-in effects refer to the artificial increment in the IDIF measurement due to the activity from the surrounding tissues spilling into the carotid region. Spill-out is the opposite effect, in which the activity measured is lower than the real one.

Due to the limited resolution of PET cameras, building a reliable completely non-invasive IDIF method has been a huge challenge. The reference method for extracting IDIF has been the one proposed by (Chen et al., 1998) in which 3 late venous blood samples are used to calibrate the TAC that has been extracted from the carotids and correct it for PVE. Several methods were proposed to avoid the necessity of taking blood samples, as for example the previous estimation of recovery coefficients using phantom studies (Croteau et al. 2010). More recently, it has been suggested that with standard resolution IDIF methods based solely on the PET data could not be considered reliable, and that late venous blood samples should be used whenever possible (Zanotti-Fregonara, Fadaili, et al. 2009). It should be noted that promising developments of technology, notably the HRRT (High Resolution Research Tomograph), allow achieving spatial resolutions better than 3 mm (Fung & Carson 2013), thus opening new doors.

Another important factor that contributes to the accuracy of the IDIF is the tracer used in the PET exam. Notably, three characteristics should be taken into account: tracer kinetics, production of metabolites, and interaction of the tracer with blood cells. The kinetics affects the signal's carotid-background ratio. This means that different tracers show different carotid signal's strengths, depending on the kinetic behavior of the tracer in the brain. Notably, whether the uptake of the tissue surrounding the carotid artery is weak or strong, slow or fast, comes into play. After administered in the patient,

tracers produce metabolites in an amount and timing which depends on the tracer. The goal when obtaining an IDIF is to measure the parent concentration of the tracer in plasma alone, but PET images do not allow distinguishing between parent activity or radiometabolites activity. While in some tracers the parent-metabolite ratio can be neglected, as for example in ^{18}F - Fluoro-2-deoxyglucose (FDG), for others its calculation is mandatory to obtain an accurate input function. The most reliable way to do this is by blood sampling, thus adding again the necessity of introducing an invasive component to the IDIF method. This may be counterintuitive, as IDIF intends to prevent the invasiveness. Nevertheless, IDIF methods introduce the advantage of at least reducing the number of blood samples used. Often it suffices to take venous blood samples, which is also advantageous (Zanotti-Fregonara et al. 2011). Avoid blood samples seems difficult for another reason. By using IDIF, it is implicitly assumed that the difference between the plasma tracer concentration and the one in whole blood is negligible. Although this is true for some tracers like ^{18}F-FDG, for many others its molecules can bind to blood cells that have specific binding sites, causing uneven distribution between cells and plasma and thus requiring determining plasma concentration of tracer.

Finally, IDIF estimation was also shown to be vulnerable to patient head movements during the PET exam (Zanotti-Fregonara & Liow 2012).

The large number of factors influencing a reliable carotid-based IDIF estimation turns this approach very difficult to successfully achieve. After years of research, there is some skepticism about considering IDIF as the solution for arterial cannulation. In fact, despite all the interest, the incorporation of IDIF in clinical research protocols as a mechanism to reduce invasiveness was quite poor. As there are so many variables which influence the reliability of the results, IDIF extraction methods should be case-specific, by fitting the technology and the tracer used.

1.3. Objective and Outline of the Thesis

The current work has the main goal of studying methods for deriving an IDIF from the internal carotid arteries, as an alternative to arterial cannulation, to perform quantification of PET images.

As mentioned above, reliable IDIF estimations typically rely on the extraction of blood samples to calibrate the carotid activity function for PVE, and determine the

parent and plasma fraction of radiotracer, which is not possible to obtain from PET data alone. This study, however, was thought to be performed completely non-invasively, in the context of the work developed in the IBILI/ICNAS, since there is no blood sampling protocol or equipment available yet. In this sense, this thesis evaluates how IDIF methods may be implemented in the ongoing projects at IBILI/ICNAS.

With this consideration, the assessment of the methods using PET data focused [^{11}C]-Raclopride images. This particular tracer, which widely used for ongoing studies, does not typically require the estimation of an IDIF because the usage of a reference region as input for the quantification models has been validated. Furthermore, there is plenty of information in the literature on [^{11}C]-Raclopride, in particular on data required to approximate the metabolites and plasma corrections. In addition, considering this radiotracer allows the possibility of evaluating the performance of IDIF methods by comparing the resulting quantified parameters to those obtained using the reference region methods.

In this context, this thesis involves the understanding of several topics.

In the second chapter the quantification methods for PET images are detailed, emphasizing the quantification methods specifically used in this work. In the third chapter, a review of the IDIF state-of-the-art is made, in which the carotid arteries' segmentation procedures will be addressed, as well as the PVE correction methods and the metabolites and plasma fraction corrections. Based on the findings of this third chapter, two totally non-invasive methods were derived and assessed in the fourth chapter. They were compared to the widely used blood sampling method which had been proposed by (Chen et al. 1998) for [^{18}F]-FDG. Finally, in chapter five, blood-free IDIF methods were applied to [^{11}C]-Raclopride PET images of 13 subjects to derive the AIF and quantifications were performed, to determine the BP. The results will be compared to the ones derived with a validated reference region.

Throughout the whole thesis, the application of invasive and non-invasive quantification methods for [^{11}C]-Raclopride will be addressed. In particular, its kinetics, metabolites production and plasma interaction will be discussed.

2. Quantification of Brain PET Images

2.1. Introduction

In a PET study, physiologically active compounds are labeled with a positron-emitting isotope and administered to the patient intravenously. Through the measurement of the annihilation radiation using a coincidence detecting technique, it is possible to track and quantitatively measure the labeled compound and study its biochemical and physiological properties *in vivo*.

After data reconstruction and correction for attenuation, scatter, dead-time, movement, partial volume effect and decay, PET images provide 4D data of radioactivity concentration (kBq/ml) as a function of time, which is assumed to be proportional to the ligand concentration. The ligand concentration in tissue is, in turn, related to the underlying processes in study. Nevertheless, PET also has the potential of providing more complex and specific information about the tracer's kinetic behavior other than its distribution in time, by isolating specific signals of interest. That potential has been explored by developing tracer kinetic models that better characterize the tracer kinetics and biological states through the determination of significant kinetic parameters. The usual measurements include the quantification of blood flow, cerebral metabolic rate of glucose, cerebral oxygen utilization and neuroreceptor ligand binding, through the determination of significant compound parameters as the metabolic rate, the distribution volume (DV) and the binding potential (BP).

In this chapter several quantification models and methods are reviewed, with special emphasis given to those that will be mentioned in Chapter 5.

2.2. Compartmental Models

The frequent starting point for PET image analysis and quantification is

assuming the ligand interaction with the physiologic system in study may be mathematically described by a compartmental model. This model assumes there are physiologically independent pools (or "compartments") of tracer, not discriminated in the PET image, and seeks to quantify the tracer concentration at each pool, as function of time (Watabe et al. 2006) The compartments should not be interpreted as representing physical volumes, but rather a homogenous mass of material that behaves uniformly, in which the tracer can assume several locations. Tracer may be exchanged between compartments and the concentration change in one compartment is often assumed to be a linear function of the concentration in the other compartments, which means the tracer exchange happens at a constant rate, described by the transfer coefficients. The number of compartments to be considered depends on the chemical and biological properties of the ligand, and also on the specificity of the analysis intended. Increasing the complexity of the model structure increases the complexity of determining the transfer coefficients to characterize the tracer's behavior.

The structurally simplest model of this kind is the one-tissue compartmental model. Tracer injected intravenously as a bolus is assumed to arrive to the capillary network of the considered physiologic zone as being well-mixed in arterial blood, and equally distributed throughout all the circulation. In this model, the tracer interaction between the arterial plasma in the capillary, C_P, and the surrounding tissue, C_T, can be represented as shown in figure 2.1.

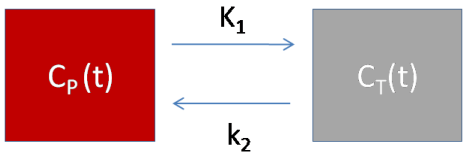

Figure 2.1 – One-tissue compartmental model. In this simple model, no further information about the radiotracer present in the tissue is provided.

The transfer coefficient K_1, expressed in units of $mLmin^{-1}mL^{-1}$, describes transfer of radiotracer from plasma to tissue and is a function of the blood flow, capillary permeability and plasma protein binding. The coefficient k_2 characterizes the efflux from tissue back to plasma, indicating the fraction of mass transferred per unit of time and is therefore expressed in units of min^{-1}. The change over time of tissue concentration in this model can be expressed by the following differential equation

$$\frac{dC_T(t)}{dt} = K_1 C_P(t) \; - \; k_2 \, C_T(t) \qquad (2.1)$$

which indicates that the tracer is transferred to the tissue from plasma in a way proportional to the plasma concentration C_P and is transferred from the tissue back to plasma in a way proportional to the tissue concentration C_T.

Solving equation 2.1 and determining the kinetic parameters K_1 and k_2 is possible by fitting the model to measured PET data with the AIF as input. The latter corresponds to the metabolite-corrected plasma concentration of tracer in time, C_P, as mentioned in section 1.2. More details about this function are addressed in section 2.6.

A more specific characterization of the behavior of tracer in the tissue, which is usually particularly sought because of the interest in assessing the binding of tracer to the pre-defined target, leads to more complex compartment model structures. In particular, the three-tissue compartmental model considers that once in the tissue, the tracer may be free (C_{T1}), specifically bound to the target molecule (C_{T2}) or non-specifically bound to other not relevant molecules (C_{T3}), see figure 2.2.

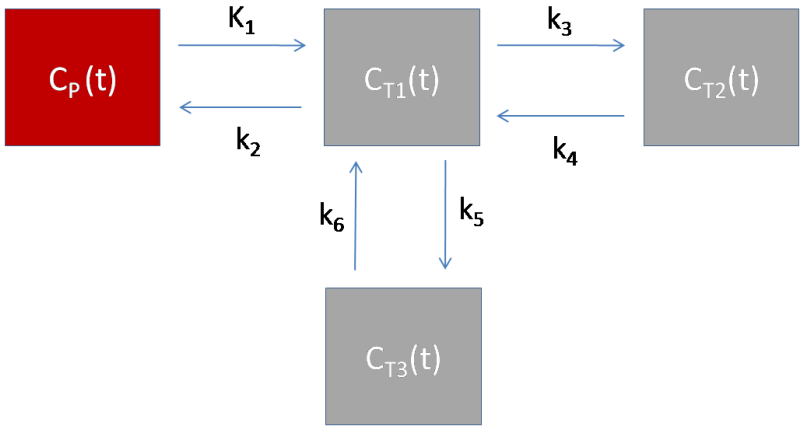

Figure 2.2 – Three-tissue compartmental model. Here, C_{T1} corresponds to the concentration of free radiotracer in tissue; C_{T2} corresponds to the concentration of radiotracer specifically bound to the target molecule; C_{T3} corresponds to the concentration of radiotracer bound to other molecules. This scheme is equivalent to the one introduced in section 1.1, however displaying the notation used throughout this chapter.

One can derive the differential equations that describe the three-tissue model likewise to what had been done for the one-tissue model. This would now lead to a more complex system of equations with six coefficients to be determined, see section 1.1. There is then an increased difficulty in determining the coefficients reliably. For

this reason, a simpler two-tissue model is used whenever possible, eliminating the non-specific binding compartment C_{T3}. This can be eliminated if the non-specific binding of the tracer can be neglected or included in the free compartment due to rapid exchange between free and nonspecific pools (Lammertsma et al. 1996). This model is represented in figure 2.3, where C_{T1} corresponds to the concentration of free radiotracer and C_{T2} corresponds to the concentration of radiotracer bound to the specific target.

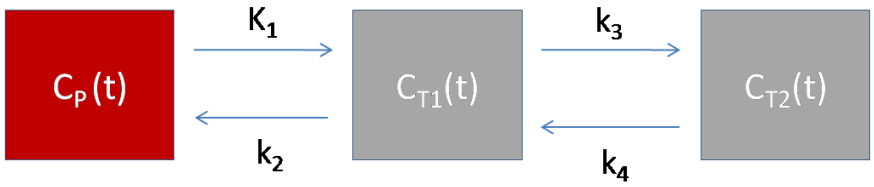

Figure 2.3 – Two-tissue compartmental model. In this model, the non-specific binding compartment is not considered. C_{T1} is the concentration of free radiotracer in tissue and C_{T2} is the concentration of radiotracer bound to the specific target.

It can be described by the following equations:

$$\frac{dC_{T1}(t)}{dt} = K_1\, C_P(t) \;-\; (k_2 + k_3)\, C_{T1}(t) + k_4\, C_{T2}(t) \tag{2.2}$$

$$\frac{dC_{T2}(t)}{dt} = k_3\, C_{T1}(t) \;-\; k_4\, C_{T2}(t) \tag{2.3}$$

The coefficient k_3 is the rate constant for transfer from free to specific binding of the tracer to a receptor (min^{-1}) and k_4 the rate constant for dissociation from that specific binding back to free compartment (min^{-1}).

A tissue ROI defined in a PET image constitutes a mix of different signals, representing the summed contributions from all tissue compartments. Considering the two-tissue compartmental model, it is then only possible to measure from PET the summed tissue concentration C_T, which comprises the free and specifically bound concentrations:

$$C_T = C_{T1} + C_{T2} \tag{2.4}$$

In addition, before determining the coefficients of the model, it is important to consider that a tissue PET ROI will also contain a significant contribution from the intravascular activity. Thus the measured tissue concentration will be affected by blood spill-over that will depend on all activity within the intravascular space, or by other words, the whole blood concentration (C_B). A blood volume component V_B, composed of small capillaries, should therefore be included in the measured ROI concentration

$$C_{PET}(t) = (1 - V_B)\, C_T(t) + V_B\, C_B(t) \tag{2.5}$$

where C_{PET} is the measured activity from a tissue PET ROI. From equations 2.2 to 2.5, the measured tissue activity C_{PET}, the plasma activity (AIF) and the whole-blood activity C_B it is possible to derive the parameters K_1, k_2, k_3, k_4 and V_B using standard nonlinear regression analysis. For the simplification of the calculations it is usually assumed the fractional volume V_B ranges approximately between 3% and 5% of the sampled ROI (Leenders et al. 1990).

Depending on the properties of the radiotracer that we're interested in studying, combinations of the transfer coefficients may provide a more meaningful analysis, and also simplifications in the calculations. For a neuroreceptor ligand, the most significant parameter is the binding potential (BP), which appears in compartmental models as the ratio between the specific binding transfer constant k_3 and the dissociation constant k_4:

$$BP = \frac{k_3}{k_4} \tag{2.6}$$

The distribution volume (DV) of a radioligand, in the context of a compartmental analysis, is defined as the ratio between the radioligand concentration in tissue target region, C_T, and the radioligand concentration in plasma C_P, at equilibrium. From the compartmental models, it is also possible to derive DV from the kinetic constants. For a one tissue compartmental model, the DV equals to

$$DV = \frac{K_1}{k_2} \tag{2.7}$$

and for a two-tissue compartmental model, the DV equals to

$$DV = \frac{K_1}{k_2}\left(1 + \frac{k_3}{k_4}\right) \tag{2.8}$$

2.3. Reference Tissue Models

Another compartmental model, alternative to those described above, is the reference tissue model, RTM, (Lammertsma et al. 1996). Again, the BP is the parameter of interest. This model does not require a plasma metabolite-corrected input function (AIF), and therefore avoids the invasiveness of arterial sampling. It uses as input the TAC of a tissue region in which one can assume there is a negligible concentration of specific binding sites, a reference region. On this reference region, it is assumed that a one-tissue model referring to plasma concentration and non-specific concentration of the tracer is enough to describe it, see figure 2.4. The concentration of radiotracer in the reference tissue is denoted by C_R. By assuming that the degree of non–specific binding is the same in the reference tissue region and in a region of interest, the kinetics of the tracer in specific binding regions can be described as a function of the reference region TAC, C_R, as is explained below.

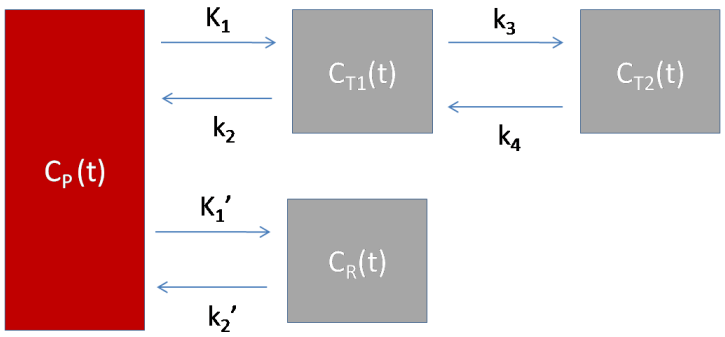

Figure 2.4 – Reference tissue model. In this model, the kinetics of the region of interest are described using as input a reference region TAC, denoted as C_R, avoiding the use of an AIF.

Equations derived from this model are equations 2.2 and 2.3, from the two-tissue model, and equation 2.9

$$\frac{dC_R(t)}{dt} = K_1{}' C_P(t) - k_2{}' C_R(t) \tag{2.9}$$

where K_1' is the rate constant for transfer from plasma to reference tissue compartment and k_2' is the rate constant for transfer from reference tissue back to plasma compartment, as described in (Lammertsma & Hume 1996). Considering equations 2.2, 2.3 and 2.4, a relationship between C_T and C_P can be derived. Moreover, from equation 2.9 which denotes a relationship between C_P and C_R, a relationship between C_T and C_R is further derived. Considering the additional assumption that the DV of compartments C_{T1} and $C_{R,}$ in the figure 2.4, is the same

$$\frac{K_1}{k_2} = \frac{K_1'}{k_2'} \tag{2.10}$$

the model can be simplified obtaining an operational equation with four parameters: R_1, k_2 ,k_3 and BP, R_1 being the ratio K_1 /K_1'. These parameters can then be obtained using C_T and C_R and standard nonlinear regression analysis. This model has been validated for [^{11}C]-Raclopride (Lammertsma et al. 1996).

(Lammertsma & Hume 1996) presented a simplification in which the tissue region of interest to quantify may be described by a single compartment, see figure 2.5. This model, the simplified reference tissue model (SRTM), only works for some tracers though, in the situations in which tracers exchange rapidly between the free (C_{T1}) and the specifically bound compartments (C_{T2}), making it difficult to distinguish between them.

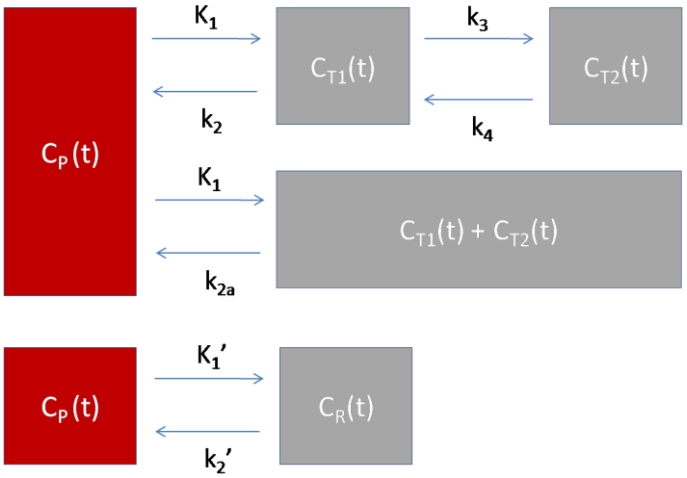

Figure 2.5 – Simplified reference tissue model. In this model, the free (C_{T1}) and the specifically bound compartments (C_{T2}) are substituted by a single compartment by assuming the kinetics between the free and specifically bound compartments are sufficiently fast.

If the above assumption is verified, which is a condition that depends on the tracer, the tissue TAC of the interest region can be fitted by a one-tissue compartment model and equations 2.2 and 2.3 can be replaced by a single equation

$$\frac{dC_T(t)}{dt} = K_1\, C_P(t) \;-\; k_{2a} C_T(t) \tag{2.11}$$

with an uptake rate constant k_{2a} equal to

$$k_{2a} = \frac{k_2}{1 + BP} \tag{2.12}$$

meaning the transfer from specific compartment to plasma. This simplification reduces the number of parameters required to describe the model to three: R_1, k_2 and BP. These can be computed from the operational equation

$$C_T(t) = R_1 C_R(t) + \left[k_2 - \frac{R_1 k_2}{1+BP}\right] C_R(t) * e^{\frac{-k_2 t}{1+BP}}. \tag{2.13}$$

where * denotes the operation of convolution, as long as C_T and C_R are known. The SRTM was also validated for [^{11}C]-Raclopride, (Lammertsma & Hume 1996).

In conclusion, the main advantages of the RTM are robustness, since there is a minor number of parameters to estimate (four), and computational speed. The SRTM only has to estimate three parameters, providing increased convergence and stability. However these models rely on some assumptions that may not work for all tracers, as the existence of a valid reference region, devoid of binding sites; the degree of nonspecific binding and the DV of the compartments C_R and C_{T1} being the same; and in addition, for the SRTM, the exchange between free and specifically bound compartment must be sufficient fast to be approximated by a single compartment. These models are also limited to the estimation of the BP and the delivery of the ligand relative to the reference region.

Despite the potential of providing a completely non-invasive quantification, by avoiding the use of an AIF, the reference tissue models can only be applied to a limited number of radiotracers. For example, the radiotracer 2-[^{18}F]-Fluoro-A-85380 is a marker for β_2-containing nicotinic acetylcholine receptors. As nicotinic receptors are

widely spread in the brain, their quantification cannot be done using a reference region, and an AIF is necessary (Zanotti-Fregonara et al. 2012). Another example of limitations of methods based on the existence of reference regions is that for [^{11}C]-Flumazenil the suitability of the *Pons* as a reference region, though it is widely used as such, has been questioned (Delforge et al. 1995).

2.4. Graphical Analysis

The graphical approaches for estimation of kinetic parameters rely on the differential equations from compartmental analysis. Instead of solving those equations to determine the individual solutions, they're rearranged into linear plots, the slopes of which represent major compound parameters describing measures of tracer binding.

This analysis can require as input function both the AIF or, if available, the uptake data from a suitable reference region C_R.

The major advantage of graphical analysis is the ease of computation when compared to finding the individual coefficients of the model differential equations. This advantage is useful for the ease of comparison among experiments when more generalist information is enough, as graphical methods work with ratios of parameters. When more specific information is sought, the individual estimation of the parameters using compartmental models is the way to follow. Another advantage of this method is not being dependent on a particular compartmental model structure; the slopes determined can be related to different combinations of parameters.

The graphical methods work differently according to whether the ligand reversibly or irreversibly bounds to the target during the scanning procedure. The Logan plot (Logan, 2000) was developed for graphically analyzing the reversible ligands, whereas the Patlak plot (Patlak et al. 1983) is focused on irreversible ligands. Raclopride is considered to be a reversible ligand, so the focus of this section will be on Logan's approach.

According to Logan's approach for reversible ligands, the graphical analysis equation can be derived from the compartmental equations describing the tracer concentration in tissue. Considering the two-tissue model, equations 2.2 and 2.3 can be rearranged into

$$\frac{\int_0^t C_{PET}(t')dt'}{C_{PET}(t)} = \left[\frac{K_1}{k_2}\left(1+\frac{k_3}{k_4}\right)+V_B\right] \times \frac{\int_0^t C_P(t')dt}{C_{PET}(t)} + int \qquad (2.14)$$

with *int* equal to, for the two-tissue compartmental model and neglecting V_B,

$$int = -\frac{1}{k_2}\left[1+\frac{k_3}{k_4}\right] - \frac{C_{T2}(t)}{k_4[C_{T1}(t)+C_{T2}(t)]}. \qquad (2.15)$$

Equation 2.14 is linear when the term *int* is constant. Usually that happens after some time instant *t*, when the compartment concentrations follow the steady state condition, in which (C_{T1}+C_{T2}) $\propto C_P$ and $C_{T2} \propto C_P$.

The slope is the total tissue DV plus the blood contribution. For a one-compartment model, the slope will be K_1/k_2, the ratio of transport constants, see equation 2.7. The DV for a two-tissue compartment (equation 2.8), which is related to the number of tracer binding sites, has been found to be estimated with much higher accuracy than individual model parameters. Another significant parameter, the distribution volume ratio (DVR), can be derived by taking the ratio between the DV from a ROI with significant number of binding sites and the DV of a reference region (devoid of binding sites), and considering the ratio of transport constants K_1 and k_2 is the same in both regions (i.e., considering equation 2.10 is valid). The DVR can then be written as

$$DVR = \frac{\frac{K_1}{k_2}\left(1+\frac{k_3}{k_4}\right)}{\frac{K_1'}{k_2'}} = 1+\frac{k_3}{k_4} = 1+BP \qquad (2.16)$$

A version of the Logan plot was derived to directly estimate the DVR using a reference tissue as input. When comparing to the SRTM, this method does not require the assumption of rapid exchange between the compartments in the target tissue, but requires an *a priori* estimate of the efflux rate constant in the reference region *k'2* (Gunn et al. 1997).

2.5. Final Notes on Quantification Methods

When adopting a model/method for PET quantification, several topics must be considered. The methods vary in terms of the output provided, the input required, the reliability of the results, the pharmacokinetics of the tracer used and computational resources required. The best choice should fit the purpose and goals of the analysis and the materials available.

Compartmental models may provide a more specific characterization of the tracer's kinetic behavior, by solving the corresponding model equations and determining the individual kinetic parameters, assuming a determined model structure provides a good description of the radioligand. Nevertheless, determining the transfer coefficients requires significant computational resources and is more vulnerable to noise in the PET measures. Solving the model equations require an AIF, which can be obtained using arterial sampling. However, this is an invasive procedure. On the other hand, the AIF may also be determined using IDIF methods. The usual problem associated to IDIF methods is obtaining a good estimation of the shape of the input function curve, especially of the rapidly changing peak. This becomes a problem when using compartmental modeling, since the estimation of the kinetic parameters is highly dependent on a good estimation of the function shape. In the literature it is common to find large and unpredictable errors associated to the individual transfer coefficients when using IDIF methods. The errors of the kinetic constants will then propagate to the compound parameters which constitute significant relationships between individual transfer coefficients and provide a more meaningful analysis, as for example the BP.

If the BP is the parameter of interest, it is possible to avoid using an AIF and resorting instead to a reference region, using the RTM or its simplified version, the SRTM. Both these models avoid the invasiveness of the arterial sampling and the obstacles of deriving a reliable IDIF, and are robust and simple to solve. Nevertheless, they only work for a limited number of radiotracers, since a reference region is not always available and it is necessary to assume some specific conditions that can only be respected by some particular tracers.

Graphical approaches provide a quick, visual estimation of compound parameters like the DV and if a reference tissue is available, the DVR, from which it is possible to derive the BP. They are a robust solution and do not need an a priori assumption of a specific model structure. They require as input an AIF, a reference region TAC or both, depending on the compound parameters sought. As in the case of compartmental modeling, to avoid the invasiveness of the arterial sampling, the AIF

may be estimated using IDIF methods. When compared to the compartmental models regarding to the use of an IDIF, the graphical methods come up being more robust to the usual IDIF errors. As these approaches only work after a certain time, in which the linearity in achieved by reaching the *equilibrium*, they do not require a precise estimation of the early part of the curve. They are more sensitive to a good estimation of the tail of the AIF, which is potentially vulnerable to bias due to the late increased production of metabolites. Better results are achieved with blood-based IDIF methods, in which some blood samples are drawn to scale the IDIF for both correcting for PVE and also for obtain an accurate measurement of the contribution of radiometabolites.

In conclusion, the literature suggests that graphical approaches are a good option when it comes to determining compound parameters. If individual rate constants are needed, compartmental modeling can solve the problem. More reliable results can be obtained using full arterial sampling than using other AIF estimation methods.

2.6. The Arterial Input Function

As previously mentioned, for many radiotracers it is not possible to find a valid reference region. Therefore, the most used input function is the AIF. In this section a brief review of the methods to derive the AIF that do not rely on the image will be made. A detailed discussion of the IDIF state of the art is available in the next chapter.

The gold-standard method for obtaining the plasma concentration of radiotracer (AIF) is arterial blood sampling. This is based on the cannulation of the radial artery, and can be performed through manual sampling procedures or automated continuous sampling, in which the blood is flowing through the tubing at a certain flow rate, passing the detectors. Arterial cannulation has rarely resulted in clinically relevant adversities. Nevertheless, it is laborious, often discourages subjects from volunteering for PET studies and involves risk or radiation exposure for the technical staff, when following manual procedures. The typical AIF can be characterized by an initial peak caused by the radioligand bolus infusion, followed by a slow, almost constant, decrease with time, forming a tail (figure 2.6).

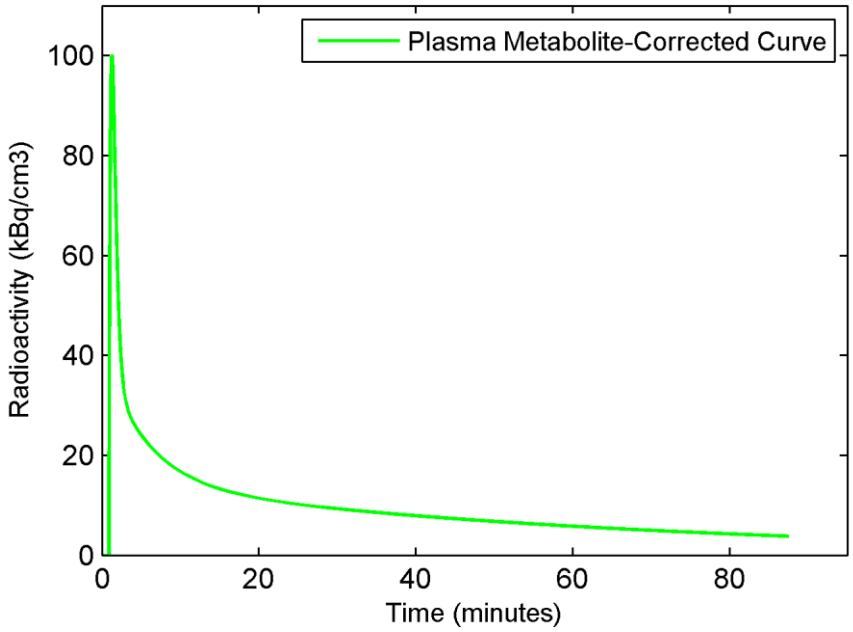

Figure 2.6 – Example of a [^{11}C]-Raclopride arterial input function, extracted from (Lammertsma et al. 1996).

The tail reflects the redistribution of the radioligand, considering the radioligand is released from tissue back to circulation. The sampling frequency should therefore be high at the beginning of the bolus injection and lower at the tail, corresponding to the later times of the exam.

It is important to emphasize that obtaining the AIF is not equivalent to determining the concentration of radiotracer in blood. After being injected in the patient's circulation, the radioligand can interact with red blood cells (RBC). This alters the tissue uptake, and therefore it is necessary to determine the plasma fraction of radiotracer that is free to cross the capillary membrane. Depending on the tracer, different interactions can occur, from not connecting to RBC to slowly or rapidly connecting to them. For the tracers that bind to RBC, the radioactivity concentration in whole blood can then be considered to be the sum of radioactivity concentrations of tracer present in plasma and tracer present in RBC, weighted by their volume fractions:

$$C_B(t) = (1 - HCT) \times C_{P\sim}(t) + HCT \times C_{RBC}(t) \quad (2.17)$$

Here, *HCT* corresponds to the hematocrit, which is the proportion of blood volume that is occupied by RBC. Usually the blood samples taken from the patient are submitted to centrifugation to separate blood cells from plasma (Oikonen et al. 2014). The plasma concentration $C_{P\sim}$ corresponds to the plasma concentration curve of radiotracer for which no metabolite correction was performed yet.

Correcting the curve for the production of metabolites is another important consideration. As the ligand interacts with the physiological mean, it can produce metabolites (by the liver, for example) that are not desired since they will not have the predefined ligand biological behavior, thus acting as a signal contaminant. Usually is assumed that the labeled metabolites can not cross the blood-brain-barrier and enter the brain tissue, but can circulate in blood. Therefore, another correction must be done, which involves determining the fraction of radioligand in plasma that corresponds to the original radioligand, the parent. The final corrected curve (AIF), corresponding to the plasma metabolite-corrected one, C_P, can be computed by multiplying the plasma concentration curve not corrected for metabolites $C_{P\sim}$ by the parent fraction, as denoted in equation 2.18.

$$C_P(t) = C_{P\sim}(t) \times ParentFraction(t) \tag{2.18}$$

According to the literature, after the centrifugation process for obtaining the tracer in plasma, typically the unchanged radioactive parent is separated using high-performance liquid chromatography (HPLC) analysis. Finally, the radioactivity concentration is performed introducing the samples in a radioactivity counter and dividing the activity by the fractional volumes.

The AIF can therefore be characterized as the plasma metabolite-corrected tracer concentration in time.

Other corrections include accounting for delay, which is related to the time the tracer takes to travel from the measuring spot (arm) to the studying tissue (the brain). It is also important to correct for dispersion, which is related to the tracer circulation, specifically to the non-homogeneous velocity fields in the vessels and in the catheter, which affects the shape of the AIF curve, especially the peak. Typically as the experimental procedure involved in the blood activity measurements contribute with a certain amount of uncertainty and it is necessary to interpolate between blood samples, an analytical function is usually fit to the blood-related measurements (Silva 2012).

As an alternative to arterial sampling, there are some other techniques validated to obtain the AIF. Population-based input function (PBIF) or simultaneous estimation of the input function (SIME) are examples of potential viable alternatives to arterial sampling.

PBIF assumes that the shape of the AIF is similar between different subjects, differing uniquely in amplitude. Based on this assumption, this method requires a previous calculation of a standard input function created by normalizing individual input functions from a group of subjects. It's possible to derive a subject specific PBIF by scaling the standard function using one or two blood samples taken from the subject. (Zanotti-Fregonara et al. 2011) compares PBIF method with IDIF. It is mentioned that unlike IDIF, PBIF is independent on partial volume effects, scanner characteristics, quality of acquisition and reconstruction algorithm, besides being faster and requiring less labor. However like in IDIF, metabolite fraction of the tracer is presented as being a weakness. In addition, as the state of disease can alter the metabolite production, a standard input function based on healthy subjects may not be transferable to a different population of patients.

As the name suggests, simultaneous estimation of the input function (SIME) estimates input function parameters simultaneously with kinetic parameters from several ROIs. This is accomplished by incorporating the input function parameters into the objective function to be optimized while modeling several ROI data sets simultaneously, aiming to recover the input function common to all ROIs. (Zanotti-Fregonara et al. 2011) emphasize that at least one blood sample must be collected to improve the parameters estimates.

2.7. Quantification and Kinetics of [^{11}C]-Raclopride

In this work, [^{11}C]-Raclopride images will be used to derive IDIFs, which in turn will be used for quantification of the images to determine the BP. In this section no exhaustive review of the use of [^{11}C]-Raclopride will be made. The main goal is to introduce the most important topics around the kinetics and typical quantification studies found in the literature.

Raclopride is a highly selective antagonist of D_2 dopamine receptors and is used in PET studies aiming to quantify those receptors in the striatum by labeling it with ^{11}C. The striatum composed by the *caudate nucleus* and the *putamen*. It has been widely

used in studies related to movement disorders and schizophrenia, to determine the efficacy of dopaminergic drugs and to visualize the changes in synaptic dopamine.

Unlike the striatum, the cerebellum is nearly devoid of D_2 receptors and it is assumed that there is negligible specific binding of the tracer in that part of the brain. This makes the cerebellum an eligible region for extracting a reference tissue input TAC. As consequence, [^{11}C]-Raclopride studies do not usually include arterial sampling procedures. Instead, a reference tissue TAC is used as input with the SRTM model, assuming Raclopride has rapid kinetics between free and specific compartments. This method has been the most popular method to derive the BP, considering it is non-invasive, has ease of computation and produces reliable of results.

Nevertheless, graphical methods for reversible tracers, the Logan plot, can be applied to [^{11}C]-Raclopride PET data using both AIF and reference cerebellum curve to produce DV and DVR estimates (Logan et al. 1996). In (Lammertsma et al. 1996) a plasma input function was used. Resorting to compartmental modeling, the BP was calculated both from deriving the individual parameters k_3 and k_4 and from DV values of striatum and cerebellum.

Since for the present work arterial blood sampling was not available, it was not possible to use blood samples to determine the unchanged fraction of tracer nor to quantify the plasma fraction. Therefore, those are obstacles that were solved by performing approximations based in the literature. We note that [^{11}C]-Raclopride has been one of the most widely used radiotracers in PET imaging, and as consequence there is a vast amount of information published.

In particular, [^{11}C]-Raclopride usually persists in plasma and does not penetrate the RBC membrane (Oikonen et al. 2014). Considering this assumption, in equation 2.17 the concentration of the radiotracer in RBC, denoted C_{RBC}, will be zero. The concentrations in plasma and blood are then related by the equation

$$C_B(t) = (1 - HCT) \times C_{P\sim}(t) \tag{2.19}$$

This means that we simply need to know the whole blood concentration C_B, which is taken from the image, and the hematocrit HCT to derive the plasma free tracer concentration $C_{P\sim}$ (as in equation 2.17, the ~ symbol denotes that no correction for metabolites is being considered yet) . Based on the normal values for the hematocrit (Oikonen 2008), henceforth we take HCT=0.5.

About the production of metabolites, the literature suggests that Raclopride has a relatively slow metabolism, and that the labeled metabolites do not cross the blood-brain barrier. Unlike most tracers, (Zanotti-Fregonara et al. 2011) mentioned that successful studies were performed with Raclopride using an average metabolite curve for metabolite correction. From this assumption, using values extracted from (Farde & Halldin 1989), in which the parent fraction was determined by measuring the unchanged tracer in arterial blood samples four and forty-two minutes after injection, a parent fraction curve was derive to be used in this work, see figure 2.7. It was assumed that the fraction of unchanged tracer was 0% at the moment of injection of the tracer, 93% four minutes after the tracer injection and 73% at 42 minutes after the tracer injection. An exponential function was fitted to those values, similarly to what had been done in (Farde & Halldin 1989).

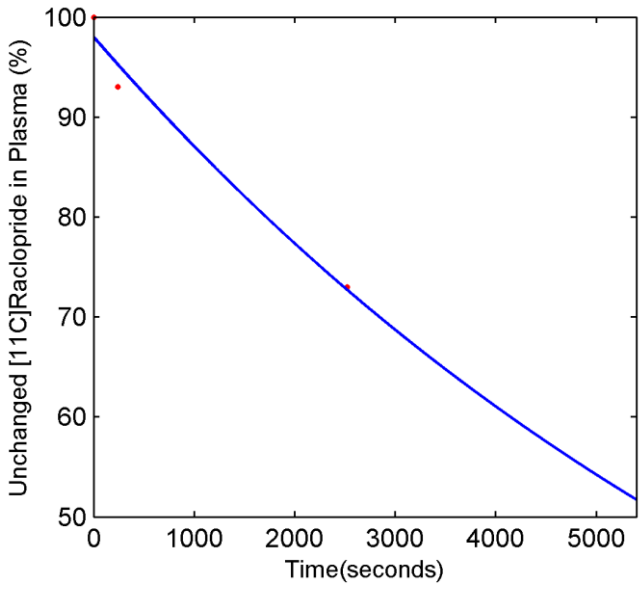

Figure 2.7 – Parent fraction curve for [^{11}C]-Raclopride determined from the literature to perform the necessary metabolite corrections in chapter 4 and 5. The red dots correspond to the values extracted from literature.

3. Image-Derived Input Function: State-of-the-Art

3.1. Systematic Review

For purposes of organization and result's quality, the contextualization of the problem was made by means of a systematic review.

Studies sustaining IDIF techniques extend for several years and many different methods, including the use of different body parts other than the internal carotid arteries as the source for the IDIF extraction. Only studies in English language involving IDIF extraction from carotid arteries, for quantification of brain PET images, and human participants were considered.

Studies reporting IDIF methods validation using carotid arteries were identified by searching the electronic database PubMed. This search was run on the 25th February, 2014. The following search string was used to identify full-text articles within the PubMed database: "(image and derived and input and function or IDIF or noninvasive) and PET and carotid". Other relevant records were retrieved by hand-searching the bibliographies of the articles meeting the inclusion criteria.

A total of 39 articles were retrieved by the search made in Pubmed. A preliminary analysis was performed on the basis of their abstracts in order to exclude those that did not meet the inclusion criteria. As a result, 22 of the previous studies were discarded for not meeting the eligibility criteria. The full texts of the remaining 17 studies were thoroughly examined. By checking the references of the 16 remaining articles, 8 additional relevant studies that met the inclusion criteria were identified.

All the final selected articles were organized and characterized according to a relevant topics' list. This list was progressively composed and built following the full-text reading. In particular, the following topics were considered for each article: article type, technology of the scanners (standard, HRRT or hybrid), radiotracer used, carotid arteries' segmentation method (PET or PET/MRI based images; manual, semi-automatic or automatic methods), type of PVE correction, correction for metabolites and plasma fraction, and finally the kinetic model used.

3.2. Typical IDIF Study

Several approaches for IDIF extraction are proposed in the literature. However, most share a number of features. Notably, the IDIF extraction process is typically composed of three steps: (1) Carotids VOI Definition and Raw-TAC Extraction; (2) Correction for Partial Volume Effects; (3) Correction for Metabolites and Plasma Fraction. These steps will be described in the following subsections.

3.2.1. Carotids VOI Definition and Raw-TAC Extraction

The first step in the IDIF extraction process is identifying the internal carotids region. This is done by manually or automatically selecting the voxels corresponding to the carotids. The concentration values in that region are then extracted throughout time.

In most papers, this is made by placing volumes of interest (VOIs) directly on PET images. In this context, for obtaining the latter, it is common procedure to use a fast image-acquisition protocol. This allows obtaining frames with short duration, which is rather relevant to characterize the IDIF in the initial time instants, where it varies the most.

Techniques for identifying carotid regions directly on dynamic PET data vary from manual to semi-automatic and automatic. Manual techniques typically start by summing the earliest PET frames, where carotid arteries are easier to identify, since the tracer hasn't already spread into the surrounding tissue. According to (Zhou et al. 2011), the relevant frames are the ones that capture the function peak. After summing the relevant PET frames a visual inspection of the data allows selecting the slices in which the arteries are visible. Usually 5 to 8 slices in the lower part of the brain are selected. Finally, the selection of the ROI in each slice can be done by applying a threshold so that voxels with intensity above its value are selected to compute the IDIF. (Chen et al. 1998) selected the voxels from the earliest frames (summed) whose values were greater or equal to the product of a constant and the highest intensity of voxels in the interest area. The constant was visually adjusted to generate the best result. The resulting ROI was copied to all frames to extract the TAC.

(Zhou et al. 2011), considered that using a subjective threshold method is not accurate enough to correctly determine the physical area of interest. Instead they purposed to use the knowledge of the behavior of TACs from both arterial and tissue

voxels to derive a semi-automatic method. It is known that arterial input function can be characterized as rapidly crescent, achieving its maximum in the first moments forming a peak, and then slowly decrescent over time, see figure 2.6. Contrastingly, tissue TAC simply slowly increases along time without forming a major peak (Zanotti-Fregonara et al. 2011). Using this features, they proposed a method which starts by manually define a 3D region containing the carotid arteries. This was made in early summed images, by manually defining a rectangle in each slice. As previously, the slices had been selected so that the arteries would be visible. The voxel selection was made by fitting a linear regression to each voxel TAC, in order to evaluate its progression along time and select the voxels that in fact reveal an input function behavior. The ones with a negative slope, translating a decrease of measured activity along time, were selected. Other approach, considered by (Jurgen E M Mourik et al. 2008), involves the use of a semi-automatic region growing method. This method requires as input a voxel threshold value and the choice of a voxel as starting seed for each carotid artery. For each seed defined, the algorithm examines whether the neighboring voxels satisfy the threshold also defined *a priori*. Iteratively, the voxels that pass the evaluation will be added to the seed, and the algorithm stops if no more voxels are added.

Automatic methods were vastly explored in the past years. Although offering promising features like avoiding the subjectivity and labor of manual ROI delineation, it's not clear whether more accurate results can be achieved when comparing to manual methods (Chen et al. 2007). Automatic methods are statistical procedures that use temporal tracer kinetics to identify carotid voxels directly on dynamic PET images. Notably, they are: k-means clustering (Liptrot et al. 2004); independent component analysis (ICA), studied by (Su et al. 2005), (Chen et al. 2007) and (Naganawa et al. 2005), that introduced their own ICA version, named EPICA; local means analysis (Zanotti-Fregonara, Maroy, et al. 2009); graph based Mumford-Shah energy minimization (Parker & Feng 2005); and non-negative matrix factorization method (Bodvarsson et al. 2006).

Identifying ROIs on PET images alone is not always simple due to their low signal-to-noise ratio and resolution. For that reason, some authors opt to co-register PET with anatomical MRI images for more precise carotid arteries definition. (Litton 1997) used MR images to manually draw carotid ROIs and then applied them directly on co-registered PET images. Though the advantages of this approach are intuitive, it also may lead to co-registration errors. (Fung et al. 2009), explained that inaccurate co-

registrations of carotids happen since co-registration algorithms operate using brain structures above carotids location. Besides, it is important to account for errors that arise from different patient's head positioning across exams. Due to the small size and elasticity of carotids, they can be bent and twisted depending on the head position, leading to alignment errors (Zanotti-Fregonara et al. 2011). Nowadays, hybrid PET/MR scanners provide the means to overcome barriers in the co-registration, as they allow performing PET and MR exams simultaneously. As this technology is not yet widely available, this work will not focus much on it.

3.2.2. Correction for Partial Volume Effects

As described above, partial volume effects (PVE) are particularly relevant in IDIF-based methods for brain PET imaging, due to the small diameter of the carotids when compared to the resolution of most PET scanners. The literature proposes several strategies to deal with this source of errors. Calibration of the TAC curves extracted from the PET data can be done by using blood samples (blood-based IDIF methods) or in a non-invasive way (blood-free methods). Particularly for the former, it is important to note that errors arising from partial volume effects are particularly relevant in the later part of the exam, as the tracer starts to accumulate in the tissue around the carotids.

The IDIF technique is meant to avoid or reduce the invasiveness of arterial blood sampling. However, drawing blood samples cannot always be totally avoided. It sometimes can, but the literature suggests that blood-free methods provide less accurate results (Chen et al. 2007; Zanotti-Fregonara, Fadaili, et al. 2009). In addition, using blood samples demonstrated to provide reliable results even if patient movement during image acquisition was present (Zanotti-Fregonara & Liow 2012). Accordingly, most IDIF methods use a reduced number of blood samples (1-3). Some propose drawing arterial blood samples (Naganawa et al. 2005), which by comparison to the gold standard only offers the advantage of reducing the number of samples to be obtained. Other IDIF methods are based on extracting venous samples to calibrate the raw-TAC, which is significantly less invasive.

The possibility of using venous blood samples for effectively computing the IDIF depends on the tracer. Tracer arterial and venous kinetics are initially different but after a period of time, arteriovenous equilibrium is achieved and venous blood can be used to calibrate the TAC. The problem is that the timing of equilibrium varies from

tracer to tracer and for some it is not achieved during the PET data acquisition timeframe. For these reasons, a standard method valid for all tracers is not available.

(Chen et al. 1998) proposed a method for PVE correction that has shown good results and also high reproducibility. In their study they used ^{18}F-FDG, which is known to reach arteriovenous equilibrium in approximately 10 to 15 minutes after injection. With that consideration, the raw-TAC was calibrated using three late venous samples extracted from volunteers. These samples were used as input for the estimation of the recovery coefficients r and s that appear in the following equation relating the raw carotid TAC values measured from the PET image $C_{measured}$, with tissue TAC values C_{tissue} and the sought IDIF, denoted by C_{real}:

$$C_{measured}(t) = r \times C_{real}(t) + s \times C_{tissue}(t) \tag{3.1}$$

Note that if no partial volume effects were present, $C_{measured} = C_{real}$. However, spill-out effects imply that the activity measured from the ROIs is decreased relatively to the real one: in the equation this implies that $0 < r < 1$. Spill-in effects from the surrounding tissue increase the measured activity: in the equation this implies that $0 < s < 1$. C_{tissue} is extracted from a ROI drawn in a region close but not adjacent to the ROI of the carotids. In a practical situation, C_{real} is sought, rather than known. Blood samples are drawn to provide an approximation for C_{real}. For the instances in which the samples are taken, r and s are determined resorting to the linear least square method. As they are considered to be time-independent, it becomes possible to finally compute the corrected IDIF:

$$C_{real}(t) = \frac{C_{measured}(t) - s \times C_{tissue}(t)}{r} \tag{3.2}$$

Several articles employing IDIF methods reproduce, sometimes with slight changes, the approach described above. (Zhou et al. 2011), proposed a variation that does not make use of the surrounding tissue TAC, hence avoiding errors that arise from the definition of the borders of the tissue. They rewrote (3.1) in the form

$$C_{measured}(t) = r \times C_{real} \times \left[1 + \frac{s \times C_{tissue}(t)}{r \times C_{real}}\right]. \tag{3.3}$$

Now, using the notation

$$P(t) = r \times \left[1 + \frac{s \times C_{tissue}(t)}{r \times C_{real}(t)}\right] \tag{3.4}$$

one obtains

$$C_{measured}(t) = C_{real}(t) \times P(t). \tag{3.5}$$

They further showed that $P = P(t)$ is approximately linear, particularly toward the end of the scan, and so the function can then be written in the form $P(t) = at + b$. A minimum of two blood samples is enough to compute $P = P(t)$ and consequently calibrate the IDIF. Also, there is no need to determine the tissue TAC.

Despite it has been suggested that blood samples are required to accurately calibrate the IDIF, some authors propose correcting the raw-TAC using only image data. However, this has proved to be a difficult task.

Noninvasive scaling usually requires an *a priori* estimation of the correction coefficients in the modeled relationship between $C_{measured}$ and C_{real}. Different experimental carotids geometries are simulated using phantoms and the constants are computed for each of these. When determining the IDIF for a new subject, the size of his carotids must then be determined. The corresponding constants from the phantom studies are used to establish a correspondence between the IDIF and the measured data (Croteau et al. 2010). The definition of the ROIs for this subject, which in turn allows estimating the size of the carotids, is then crucial for this approach. At the same time, it can be seen as a weakness, since even small disturbances in this step potentially lead to significant errors in recovery coefficient's estimation (Zanotti-Fregonara et al. 2011). Additionally, phantoms do not exactly reproduce the shape of the carotid arteries, introducing other sources of errors.

One other approach proposed to avoid blood samples is based on the assumption that the hottest (highest-valued) voxels from inside the carotid are free of partial volume effects. (Su et al. 2005) adopted the approach proposed by (Chen et al. 1998). In equation 3.1, C_{real} was approximated by the maximum frame-wise voxel value of the blood vessel component (the last found using ICA), over the first 30 minute interval, considering the signal to noise ratio is higher. Similarly, (Parker & Feng 2005) used the

maximum value over the internal carotid ROI automatically segmented using the Mumford-Shah algorithm, as an arterial approximation. Using the maximum voxel values is an attractive alternative for the simplicity of its application. However, its use usually relies on images obtained with improved reconstruction algorithm and fine-tuned imaging features.

3.2.3. Correction for Metabolites and Estimation of the Plasma Fraction

Obtaining the arterial plasma input function using exclusively imaging methods does not allow discriminating between the parent compound and its radioactive metabolites, nor between the tracer free in plasma and that bound to blood cells. Some tracers do not require this type of correction, as for example ^{18}F-FDG. This particular tracer has a high parent-metabolite ratio and the difference between the plasma concentration and the one in whole-blood is negligible (Zanotti-Fregonara et al. 2011). Nevertheless, almost all tracers used in brain imaging produce considerable amounts of radiometabolites and many interact with blood cells.

According to the literature, estimating the unchanged radioactive parent reliably typically involves the use of arterial blood samples and high-performance liquid chromatography (HPLC) analysis The plasma concentration is measured after centrifugation of the blood samples (Schain et al. 2013). Therefore, usually some arterial blood samples are introduced in the IDIF procedure to determine the metabolite parent fraction and the concentration in plasma. The number of blood samples required to successfully determine the parent fraction seems to be dependent on the complexity of the parent fraction curve. Again, using arterial blood sampling diminishes the practical utility of the method. The only advantage would be a reduced number of arterial blood samples. (Jurgen E M Mourik et al. 2008) used the collection of seven manual arterial blood samples throughout the PET exam, while (Sanabria-Bohórquez 2003) used six and (Schain et al. 2013) used five, all for [^{11}C]-Flumazenil studies. (Zanotti-Fregonara & Liow 2012) used four arterial blood samples to both correct the IDIF for partial volume effects and obtain the parent concentration for [^{11}C]-(R)-Rolipram, by fitting a monoexponential function through the parent/whole-blood ratio calculated using HPLC analysis in the four blood samples.

Using arterial blood samples reduces the practical advantage of IDIF, so the possibility of using late venous blood samples for metabolite correction is analyzed in (Zanotti-Fregonara et al. 2011). It is mentioned the need to validate this approach for each tracer, since the parent and radiometabolites concentration along time in arterial and venous blood differs from tracer to tracer. It is mentioned that for some tracers, like the case of [^{11}C]-(R)-Rolipram, even after reaching arteriovenous equilibrium (when the radioactivity measured is the same in arterial and venous blood) the parent-metabolite fraction in arterial blood is still different from the one in venous blood , invalidating the use of late venous blood samples for that specific case.

To avoid the use of arterial blood samples is possible to resort on an average metabolite curve. However it is important to account for a big variability of metabolites production among subjects, due to physiological characteristics or any external agent like disease or therapeutic agents that affects tracer's metabolism. According to (Zanotti-Fregonara et al. 2011), an average metabolite curve cannot be used for most tracers.

3.3. Recent Technologies

The standard PET scanners used are associated with limited spatial resolution, constituting a major obstacle to the reliability of IDIF, due to a high level of PVE. As the carotids are small diameter structures with complex hemodynamic patterns, the resolution of the imaging system plays an important role in IDIF measurement.

Technological advancements in acquisition hardware and image reconstruction software lead to the development of dedicated head scanners with improvements both in sensitivity and resolution. Most recent IDIF studies are based on images produced with the High Resolution Research Tomograph (HRRT). This is the state-of-the-art system for human brain PET imaging (Schain et al. 2013), and has a spatial resolution of approximately 2.5 mm, in comparison to the 6 mm of the standard machines (Zanotti-Fregonara & Liow 2012). In addition to improved resolution, an extended field axial field of view allows a larger proportion of the head and neck region to be covered in PET images.

Despite the higher resolution of this new technological solutions, spill-in and spill-out effects still influence quantitative analysis of small structures and must be taken into account (J. E M Mourik et al. 2008). (Zanotti-Fregonara & Liow 2012) also

mentions higher vulnerability to movements during the exam than with using standard PET scanners, mostly because in the HRRT carotid arteries are sampled by smaller voxels and are delineated by smaller ROIs. In that study, a blood-based method that uses four blood samples to calibrate the function according to the method proposed by (Chen et al. 1998) achieved minimized vulnerability to motion artifacts. In the study (Schain et al. 2013) it is presented a different approach to derive the IDIF, based on the calculation of the Pearson correlation coefficient between the time activity curves of voxel pairs in the HRRT PET images to localize voxels displaying blood-like behavior.

Another important reference is the hybrid scanner 3TMR-BrainPET (Herzog et al. 2011), which allows to simultaneously obtain MRI and PET images of the human brain. This scanner provides high-resolution anatomic and functional images without the usual co-registration errors derived from non-simultaneous acquisition. In the study (Nuno da Silva et al. 2012), IDIF is derived from 3TMR-BrainPET by drawing the carotid VOIs on MR images and then copying them to the PET images. It was considered the average of values inside the VOI, the four hottest voxels per place and the four hottest voxels of the VOI to compute the raw-TAC. Venous blood samples were used to calibrate the function.

3.4. Summary

The years of research in this field suggest that the concept of extracting the AIF from image completely non-invasively is limited to particular situations. The main reason is the large number of sources for errors that lead to unreliable estimations of the IDIF, being the most important the noise of the PET images, the PVE, the metabolites production of the radiotracer, the interaction of the radiotracer with blood cells and patient movement. These errors can be in most cases corrected by using blood-based IDIF methods, which require the extraction of some blood samples. Nevertheless, the possibility of using venous blood sampling for some radiotracers, which can be considered less invasive than arterial sampling, and the use of a reduced number of blood samples can be seen as an improvement to full arterial blood sampling.

The different properties of each radiotracer are an obstacle to the reproduction of the IDIF methods, which should be validated for each radiotracer individually.

4. Numerical Simulations Using a Computational Phantom

4.1. Introduction

In the previous chapter a revision of several techniques for extracting IDIFs from PET images was made. Here, some of those techniques will be assessed by testing them on a simple computational phantom.

As the literature suggests, IDIF methods that rely exclusively on image (blood-free) do not ensure reliable results. There is a need to extract some blood samples to correct the extracted whole-blood TAC for PVE. Nevertheless, completely non-invasive methods may work under some circumstances. We note that only non-invasive methods will be used to quantify [^{11}C]-Raclopride PET data in chapter 5, as blood sampling was not available.

In this chapter, we explore both non-invasive methods and methods based on venous blood samples. The main goal is to better understand how the methods work, identify strengths and weaknesses, understand what should be the expected differences between blood-free and blood-based techniques and search for a good approach to use on [^{11}C]-Raclopride PET images, described in the following chapter.

4.2. Materials and Methods

In this chapter, we propose a computational phantom to assess some IDIF methods. In this section, first the phantom geometry and the concentration of radiotracer within it are defined. Subsequently, the methods that will be used to extract the input function from the phantom image data will be described.

4.2.1. Computational Phantom

In the literature, the internal carotid arteries ROI selection is made in an area prior to the brain, to avoid spill-in effect from the spread radiotracer in the brain area

(Jurgen E M Mourik et al. 2008). A few planes below the Circle of Willis the internal carotid arteries assume a consistent simple, straight shape, similar to a cylinder, and are easier to identify, see figure 4.1. This section of the internal carotid artery corresponds to the cervical segment.

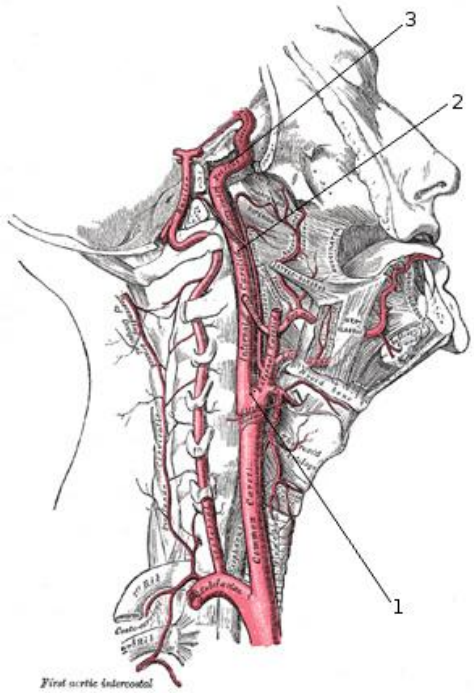

Figure 4.1 – Anatomic illustration of the internal carotid artery. After the bifurcation of the common carotid artery into the external and internal carotid artery (1), the internal carotid artery assumes a rather constant shape, the Cervical segment (2), until it curves to form the Petrous segment (3). Image adapted from (Gray 1918).

It is reasonable to assume that a geometrically simple phantom should be able to capture the relevant features of that portion of the carotids, at least as a first approximation, while still providing a highly controllable model.

We propose a simple computational phantom meant to represent a portion of one carotid artery below the Circle of Willis (Cervical segment) corresponding to only 5 slices of the PET image. The phantom is characterized by its geometry and by the time varying concentration of radiotracer within each voxel. A 23x23x5 matrix of voxels is considered for each time frame. Each voxel of the simulated PET image is assumed to be a cube of side length 2 mm, see figure (4.2). The carotid artery is simulated with the shape of a cylinder with 5 mm of diameter. Two different regions are then contained in the phantom: the carotid artery and the surrounding zone. Values of concentration of radiotracer have to be assigned to each voxel within the phantom. For that purpose,

perfect concentration curves were generated using compartmental models and resorting to [^{11}C]-Raclopride PET data reported in the literature. Three concentration curves were generated: an uncorrected whole-blood curve (C_B) for the carotid area expressing the values of concentration of radiotracer in blood, a high-binding tissue curve (C_{HIGH}), and a low-binding tissue curve (C_{LOW}), to simulate two different situations for the tissue surrounding the carotid arteries.

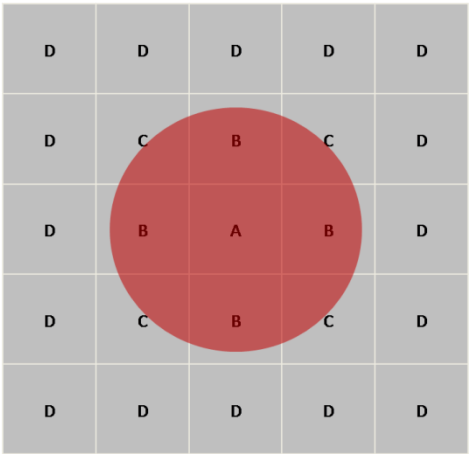

Figure 4.2 – Central 5x5 voxels of one slice of the phantom. The circle is a section of the cylinder that represents the carotid artery.

Table 4.1 – Percentage of blood and tissue concentrations assigned to the voxels of the phantom.

Voxel	% Blood	% Tissue
A	100	0
B	0.7159	0.2841
C	0.2613	0.7387
D	0	100

The central voxel of each slice of the computational phantom is assumed to be fully inside the carotid, so the radiotracer concentration within is that of blood (C_B). Voxels that contain solely tissue were all simultaneously assigned a radiotracer concentration equal to that of tissue. Two situations were simulated: in one, the concentration in these voxels was assumed to be C_{LOW} whilst in the other it was assumed

to be C_{HIGH}. For the voxels which contain both carotid and tissue, their TACs were computed as a weighted average of blood concentration and tissue concentration, according to the areas of tissue and carotid inside the voxel, see table 4.1.

The starting point for generating the perfect concentration curves was a plasma metabolite-corrected concentration curve for [^{11}C]-Raclopride, C_P, displayed as a plot in (Lammertsma et al. 1996), together with kinetic parameters for high-binding and low-binding regions (Farde & Halldin 1989). To extract numeric values from the plasma curve reported in the literature, the figure was loaded from the article into Matlab (The Mathworks, Inc., USA), where a script was created to extract the coordinates of the TAC. These coordinates were fitted with the following curve model proposed by (Feng et al. 1993)

$$y(t) = [A_1(t) - A_2 - A_3]e^{\alpha_1(t)} + A_2 e^{\alpha_2(t)} + A_3 e^{\alpha_3(t)} \qquad (4.1)$$

from which the values of C_P were extracted for t=i seconds, i=0, ..., 5400. While the plasma curve (C_P) is the relevant input for compartmental models, what can actually be directly extracted from PET data is the concentration in blood (C_B). As seen in section here are two factors to take into account when relating C_P with C_B: metabolites and the volume fraction of red blood cells. Using equation 2.18 and 2.19, it is possible to derive the relationship between C_P and C_B. The parent fraction curve already determined in section 2.7 was used to correct for metabolites. The whole-blood curve C_B can then be obtained by

$$C_B(t) = \frac{C_P(t) \times (1 - HCT)}{ParentFraction(t)} \qquad (4.2)$$

where *HCT* corresponds to the hematocrit, the volume fraction of red blood cells in the blood, and it was assigned the value 0.5 (see section 2.7).

The equations above allow computing the C_B curve required to create the phantom. Both low-binding and high-binding curves are also sought. To simulate a low-binding curve, kinetic constants of the cerebellum, a receptor-free region, taken from (Farde & Halldin 1989), were used. According to the models presented in chapter 2, due to the low-binding nature of the cerebellum, a simple one-tissue model can describe it. Solving equation 4.3 yields the concentration of the reference region C_R

$$C_R(t) = K'_1 \int_0^t C_P(t) \times e^{-k\prime_2 \times (t-\tau)} d\tau \quad (4.3)$$

Here K'_1= 0.113 and k'_2 = 0.271 are the kinetic parameters for this model, and C_P is the plasma curve, as before. The low-binding curve we seek will correspond to the concentration over the reference region. However the curve determined that way is not exactly the one that would be taken from a PET image, since the latter is affected by blood spill-over, which can be described by the equation 2.5. Applying this equation, one obtains

$$C_{LOW} = (1 - V_B)\, C_R(t) + V_B\, C_B(t) \quad (4.4)$$

in which C_{LOW} is the final low-binding tissue curve applied to the phantom and V_B is the volume of blood, which can be considered to range between to 3 and 5% (Leenders et al. 1990).

Finally, to simulate a high-binding curve, kinetic constants of the putamen, where there is high density for target receptors for Raclopride, were used, also taken from (Farde & Halldin 1989). Considering the two-tissue compartmental model described in the previous chapter, solving equations 2.2 and 2.3, it's possible to calculate C_{T1} and C_{T2}. To compute C_{HIGH}, this model was solved using finite differences. Data from the PET image does not allow discriminating between C_{T1} and C_{T2}, and like above, it is necessary to consider blood spillover. Therefore from equations 2.4 and 2.5 the final curve C_{HIGH} can be shown to be equal to

$$C_{HIGH} = (1 - V_B)[C_{T1}(t) + C_{T2}(t)] + V_B\, C_B(t) \quad (4.5)$$

Thus far, we have not mentioned which framing sequence was considered when setting up the phantom. It is the same one that had been used in the acquisition of the [^{11}C]-Raclopride PET images analysed in the next chapter. There are a total of 30 frames in the phantom, with the following durations: 4 x 15 s, 4 x 30 s, 3 x 60 s, 2 x 120 s, 5 x 240 s and 12 x 300 s. For obtaining the discrete values of the concentration of each frame from the concentration curve points determined earlier, the concentration values were averaged out within the frames. The plasma metabolite-corrected curve and the generated perfect curves used in the phantom are represented in figure 4.3. Three

points are also represented in the red line corresponding to the whole blood curve. These represent the time points where concentration values will be extracted to calibrate the IDIF. These values correspond to those that would be available in methods that draw blood samples from patients. Data in the literature suggested that arteriovenous equilibrium is reached 40 minutes after administration of the radiotracer (Bossong et al. 2009).

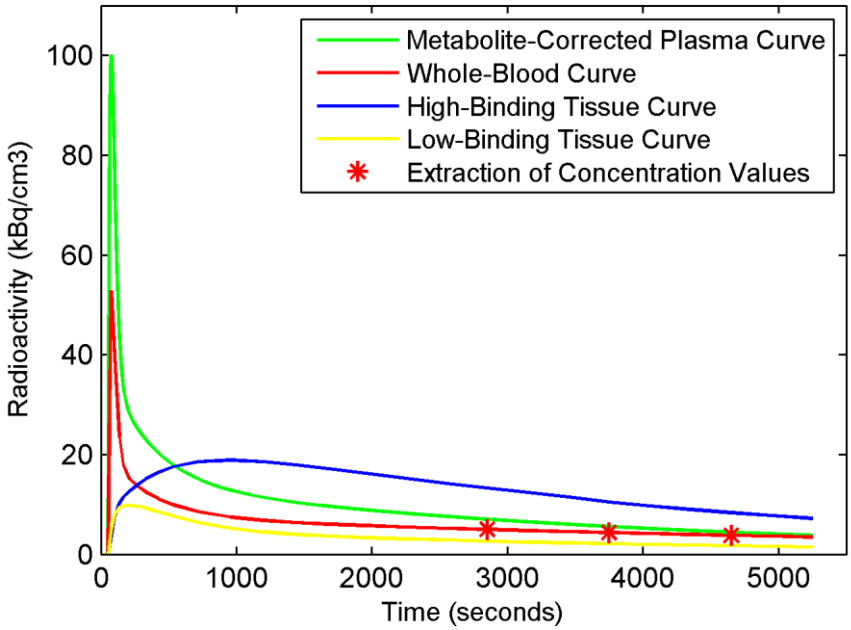

Figure 4.3 – Plasma metabolite-corrected concentration curve extracted from literature (green line); Generated whole-blood concentration curve (red line), with the times used for taking blood samples signaled with *; generated high-binding tissue curve (blue line); generated low-binding tissue curve (yellow line).

Finally, noise was added at each voxel of the phantom. The noise model was adopted from (Varga & Szabo 2002). For a given frame, its standard deviation is given by

$$SD = \sqrt{\frac{n \times C}{\Delta t}} \tag{4.6}$$

where n is a constant that determines the noise level; Δt is the length of the frame; C is the noise-free concentration value for that frame. In the literature n varies between 0.5 and 2.8.

The final noisy voxel concentration C_N is equal to

$$C_N = C + SD \times G(0,1) \quad (4.7)$$

where *G(0,1)* is a pseudo-random number from Gaussian distribution with zero mean and standard deviation of one. Finally, after adding the previous noise, the phantom was filtered with a 3D Gaussian filter for each time frame.

The phantom set up, though quite simple, is meant to allow testing the fundamental problems in extracting an IDIF. This approach is meant to yield a workable approximation of reality. The availability of a reference solution allows estimating the error associated to each method and then comparing them. Naturally, the simplifications assumed for the phantom come at a price. In particular, the geometry of real life carotids is more complex than a simple cylinder and the compartmental models are an approximation of reality. Still, preliminary conclusions can be taken from results obtained using this simplified model and checked later increasing the layers of complexity, and by working with real data.

4.2.2. Blood-Based Methods

In the previous chapter we reviewed methods for extracting the IDIF from PET images. The starting point was looking into the widely reproduced method proposed by Chen (Chen et al. 1998). This is a method we will use to extract the carotids TAC from the phantom data. Recall this method consists of summing the earliest frames where the tracer concentration reaches its peak, visually identifying and selecting the ROIs corresponding to the carotid arteries for slices where they are visible and extracting the raw-TAC using those ROIs by averaging the TACs of the voxels within them. At the same time, a tissue ROI is defined in a region close but not adjacent to the carotids ROI. Subsequently, a PVE correction is applied, in which three late venous blood samples are used to determine the time-invariant correction coefficients r and s, according to equation 3.1. In the current study the 3 late venous blood samples are simulated using 3 late values from the known generated C_B curve as reference for calibration, see figure 4.3. After determining the correction coefficients, the raw-TAC is corrected for all frames according to equation 3.2, yielding the PVE-corrected TAC.

Different voxels are differently affected by PVE and this is not taken into account by the method proposed by Chen. As an alternative novel approach, we propose

individually calculating the weight contribution of each voxel from a 3x3 ROI centered in the carotid artery. We will refer to this new method as the "Weights method", for the sake of simplicity and clarity, see figure 4.4.

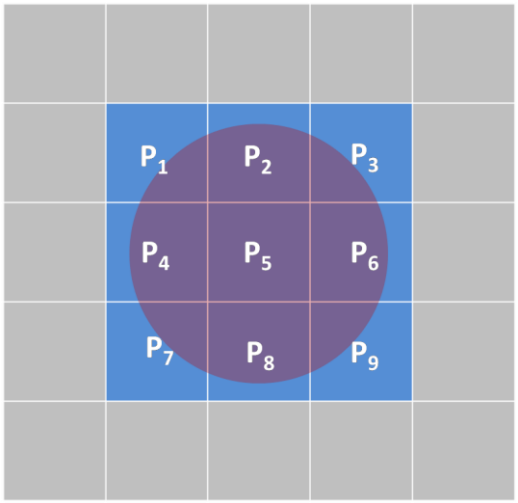

Figure 4.4 – Illustration of the Weights method. P_1, …, P_9 are the sought weights.

We will consider the carotid VOI is composed by five ROIs drawn in five slices, each one consisting on a 3x3 ROI centered in the carotid. We assume the true concentration value is the weighted sum of the intensities of the voxels over each slice ROI and that the contribution of the voxels is invariant of the slice. In other words, for each of the 5 slices and for time instant t_k, the weighted sum of the intensities of the voxels gives the real concentration value of the carotid at that time:

$$P_1 \times I_1^1(t_k) + \ \ldots \ + P_9 \times I_9^1(t_k) = C_B(t_k) \tag{4.8}$$

Here, $I_i^j(t_k)$ corresponds to the intensity value of the i^{th} voxel on the j^{th} slice at time t_k. The Weights method requires computing a 3x3 weights matrix that contains information of each slice of the VOI, see figure 4.4. This calibration procedure will be similar to that used by Chen in his method, in the sense that venous blood samples will be used as estimates for the real arterial concentration values. So using 3 late values from the known generated C_B curve as reference for calibration, the weights P_i (i=1, …, 9) can be computed from the following system of equations using least squares:

$$\begin{bmatrix} I_1^1(t_1) & \cdots & I_9^1(t_1) \\ \vdots & \cdots & \vdots \\ I_1^5(t_1) & \cdots & I_9^5(t_1) \\ I_1^1(t_2) & \cdots & I_9^1(t_2) \\ \vdots & \cdots & \vdots \\ I_1^5(t_2) & \cdots & I_9^5(t_2) \\ I_1^1(t_3) & \cdots & I_9^1(t_3) \\ \vdots & \cdots & \vdots \\ I_1^5(t_3) & \cdots & I_9^5(t_3) \\ 1 & \cdots & 1 \end{bmatrix} \times \begin{bmatrix} P_1 \\ P_2 \\ \vdots \\ P_9 \end{bmatrix} = \begin{bmatrix} C_B(t_1) \\ \vdots \\ C_B(t_1) \\ C_B(t_2) \\ \vdots \\ C_B(t_2) \\ C_B(t_3) \\ \vdots \\ C_B(t_3) \\ 1 \end{bmatrix} \quad (4.9)$$

The last equation in this system, corresponding to the last line of the matrix which has been filled with the number 1, expresses that weights sum up to one. It is, in this sense, a normalization. After the 3x3 matrix of time-independent weights has been determined, it is applied to all frames to extract the IDIF. The final IDIF value for each frame is computed by multiplying (element-wise) the weights matrix by the 3x3 matrix corresponding to the averaged 3x3 ROIs of all the 5 slices that constitute the VOI.

4.2.3. Blood-Free Methods

Most IDIF methods found in literature require drawing blood samples to calibrate the input function. Nevertheless, as mentioned in the previous chapter, it is possible to find completely non-invasive studies. Those studies rely on the determination of correction coefficients from physical phantoms or considering that a number of hottest voxels in the carotid area would be less affected by PVE and could therefore be assumed as an approximation of the real radiotracer concentration and serve as a reference for calibration.

In particular, (Su et al. 2005) used ICA to extract IDIF from [^{18}F]-FDG PET images without using any blood sampling procedure. For the PVE correction, they adapted Chen's approach, defined in equation 3.1. The first 30 minutes of the true AIF were approximated by the first 30-min TAC of the maximum voxel value in the dynamic blood-vessels component images determined by ICA. The correction coefficients were calculated and finally the entire input function was approximated. The early frames were chosen for the PVE correction assuming at those instants the signal to noise ratio is higher, hence providing better ICA results.

(Parker & Feng 2005) supported that the PVE are related to the reconstruction algorithm used and that using filtered back-projection, when compared to an iterative expectation maximization (EM) algorithm, leads to worst estimates of the recovery coefficients. After proceeding to the reconstruction of the images with an EM algorithm, they used the higher 5% voxels over the internal carotid ROI as an "accurate but noisy estimate" of the true value of the arterial input function.

Another study that used hottest voxels values was (Jurgen E M Mourik et al. 2008). In this study, the hottest four voxels per plane within the carotids from 15 to 45 seconds after the injection were selected to constitute the ROI of the carotid. Nevertheless, this approach is also performed after an improved reconstruction algorithm.

In the present work, it was not possible to use physical phantoms, nor work with improvements to the reconstruction algorithm. Therefore, the focus was instead placed on the techniques that use hottest voxels as good estimates of the true arterial input function. From the studies mentioned above, two methods were derived and tested in this phantom study, envisioning the future work with real [^{11}C]-Raclopride images.

The first method consists of a hybrid combination of Chen's method and Su's method. The carotid segmentation and PVE correction follow Chen's approach but instead of using late venous blood samples as real approximation values for three frames, we used the hottest voxel inside the carotid VOI drawn for each of three frames that cover the input function peak, from whose the correction coefficients were derived. The carotid VOI is composed by the ROIs drawn in each slice. There are some reasons for considering peak-coincident frames to derive the correction coefficients, instead of late ones, as Chen has done. The main reason is to obtain a better peak definition, which is important for the image quantification accuracy. In addition, at those frames it is easier to distinguish carotids from tissue in the PET images; as well as to detect a meaningful hottest voxel. Also (Parker & Feng 2005) mentions the possibility of in later times the maximum of the internal carotid artery be overestimated due to spill-in from the surrounding tissue, if the surrounding tissue activity assumes higher values than the carotids activity. For the sake of simplicity, we will refer to the method mentioned in the current paragraph as the Hybrid Chen (HC) method.

The second method consists on the selection of the four hottest voxels in the carotid VOI drawn in the summed over image, assuming they are PVE-free, and

averaging them for each frame to extract the IDIF in the whole image. It will be referred to as the Hottest Four Voxels (H4V) method.

The HC method, by relying on the hottest voxel, has the advantage of being closer to real values than H4V method and is expected to diminish the underestimation of the input function, which naturally occurs when considering more voxels without correcting them for spill-out using blood samples. However, the HC method is more sensitive to noise in the image than H4V.

We chose not to use automatic segmentation methods since literature suggests no significant difference was found between ROI values and quantification results using automatic or manual segmentation (Zanotti-Fregonara, Maroy, et al. 2009). In addition, the problem of not having blood samples and consequently extracting PVE affected data persists. Therefore we opted for simpler to implement and control manual segmentation.

4.2.4. Simulations

As stated earlier, typically blood samples are drawn to calibrate the carotid TAC extracted from the PET data. However, blood samples are not always available. In what follows, we assess the aforementioned blood-free methods and the widely reproduced blood-based method, Chen's method. In addition, the purposed Weights method will be compared with the latter to investigate in which way this can be a better solution for future work.

The starting point for this simulation is the computational phantom we have proposed. As the concentrations of the voxels within were generated using compartmental models, reference solutions are available, allowing the determination of the errors resulting from the application of the different methods. Three parameters are to be considered in the simulations: the activity of the tissue surrounding the carotid, the characteristics of the carotid VOI and the level of noise in the image.

As had been mentioned above, two different TACs were assigned to the voxels surrounding the carotid, corresponding to the high-binding and low-binding concentration curves C_{HIGH} and C_{LOW}, respectively. Assessing these two different situations is important as calibration typically relies on blood samples drawn at later times. Tissues with concentration curves C_{HIGH} behave differently for latter times than those with concentration C_{LOW}, which is why it important to consider how the calibration deals with different types of curves. In particular, the spill-in and spill-out

effects will be differently characterized in the PVE correction, and this study intends to simulate the different possibilities.

Another factor to take into consideration is the size of each ROI drawn around the carotid and the number of slices used for that purpose, or by other words, the number of slices that constitute the final VOI.

Different noise levels were also considered. In particular, different values were taken for the standard deviation proportionality constant n in formula 4.6 which was made to vary between 0.5 and 10, by considering steps of 0.1. For each value of n, the process of adding random error to the perfect curves, generating a phantom, applying the IDIF methods and determining the corresponding error was repeated 100 times.

Finally, the error associated to the application of a method to a phantom was assumed to be well characterized by the difference between the C_B curve extracted from the carotid and the true C_B curve introduced in the phantom to create it. The peak error (typically the most difficult region to correctly extract) and the tail error between those curves are the parameters we will look into. We define the former as being the relative difference between the maximum values between the two curves, the reference curve being subtracted. The latter is defined as the average relative difference between the curves, between t=700 and t=5400. For each error level, the differences are averaged over the 100 values corresponding to the different realizations of the noise.

All the simulations were made using Matlab (The Mathworks, Inc., USA).

4.3. Results

In subsection 4.2.1, we proposed a computational phantom as a starting point to comparing performances between the IDIF methods addressed in 4.2.2 and 4.2.3. The aspects and parameters analyzed were laid out in subsection 4.2.4.

We start by evaluating how the blood-free methods H4V and HC, described in 4.2.3, differ from Chen's method. For this purpose, we use both versions of the aforementioned computational phantom where the tissue surrounding the carotid is assumed to be of high-binding and where it is assumed that there is low-binding in that region. Figure 4.5 shows the errors associated to Chen's method (blue), the H4V method (green) and the HC method (red), both in the peak region and in the tail region. These are plotted as a function of n, the parameter related to noise in equation 4.6. As described above, for each value of n and for each method 100 phantoms with high-

binding tissue and 100 phantoms with low-binding tissue were generated. They all stem from the arterial concentration curve – the exact solution – we described extracting from the literature in subsection 4.2.1 and the subsequence C_{HIGH} and C_{LOW} curves. By applying the three methods (Chen's, H4V and HC) to each phantom and comparing the estimates for the IDIFs with the exact solution, the errors associated to the methods are computed.

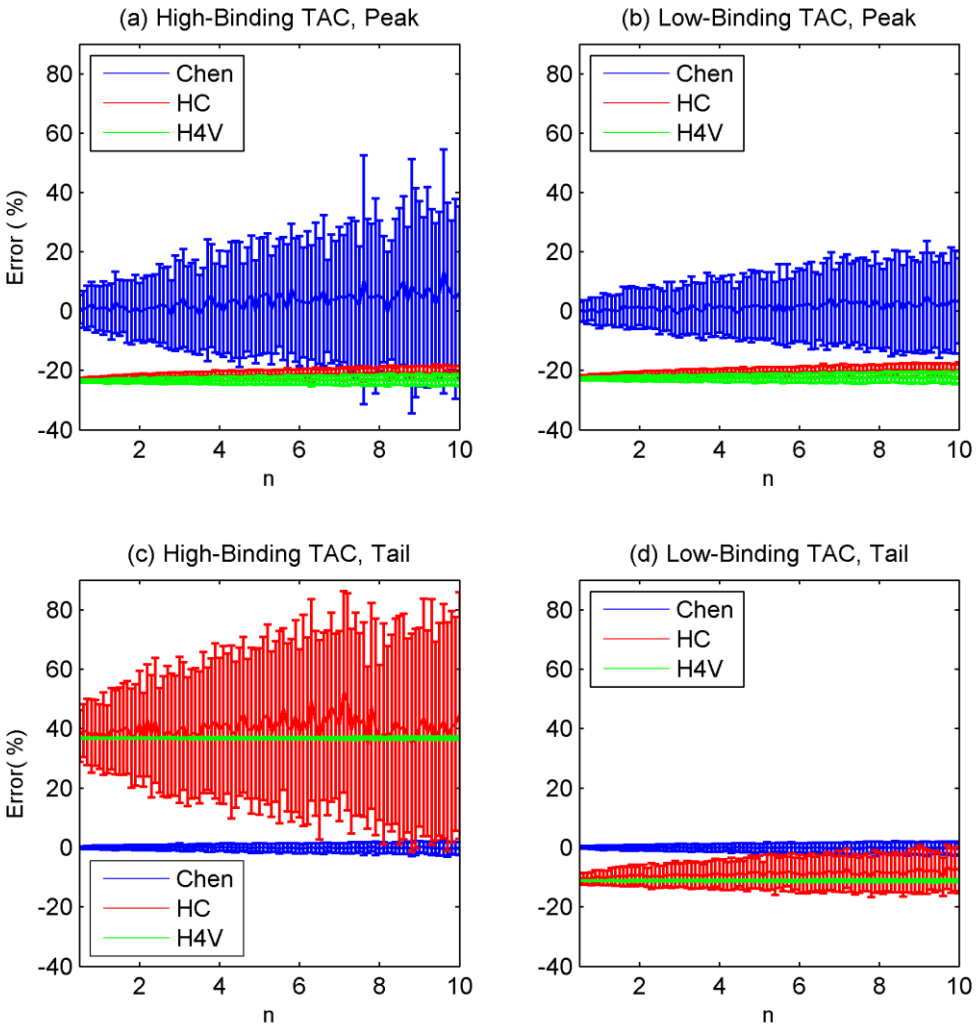

Figure 4.5 – Average error and standard deviation of the extracted TACs for 100 phantoms as function of the noise parameter n, for blood-based Chen's method (blue) and for the blood-free HC method (red) and H4V method (green). Plot (a) concerns the extracted TACs' peak error and (c) the TACs' tail error when using the C_{HIGH} tissue curve to fill the voxels around the carotid; Plot (b) concerns the extracted TACs' peak error and (d) the TACs' tail error when using the C_{LOW} tissue curve to fill the voxels around the carotid.

Evaluating Chen's method performance alone, the peak seems to be more sensitive to error variation than the tail, both in term of the magnitude of the average

differences and the corresponding standard deviations. This makes sense, since the blood samples used for calibration are drawn in later times and therefore the calculated time-invariant correction coefficients can be expected to offer a better characterization of the tail rather than the peak of the concentration curve. Blood-free methods seem to be more robust to noise level variation (n) in the peak, and provide lower standard deviations, but both of them underestimate the peak true values by around 20%, see figure 4.5(a) and figure 4.5(b). When considering the tail, results overestimated by around 40% were achieved with both blood-free methods for the phantom filled with high-binding tissue surrounding the carotid, see figure 4.5(c). A better result was achieved using the low-binding tissue curve for both methods, achieving an underestimation of less than 20%, see figure 4.5(d).

Focusing on comparing the blood-free methods between each other, one notices that despite similar underestimations of the peak, the HC method produce slightly less underestimated results. When it comes to characterizing the tail of the concentration curve for the phantom filled with high-binding tissue surrounding the carotid the HC method performed worse than the H4V because besides the similar overestimation of 40% also has a high standard deviation, see figure 4.5(c). On the other side, when using a low-binding tissue curve, errors associated to the HC method produced were found to be closer to zero than those of the H4V method, see figure 4.5(d).

In figure 4.6 the average and standard deviation of the determined correction coefficients r and s by both the HC and Chen's method, for the same simulation that lead to the results exposed in figure 4.5, are represented. It is possible to notice that the r and s coefficients don't vary much both in average and standard deviation between high-binding or low-binding curves for the HC method. That is possibly related to the fact of in the early frames, where the coefficients are determined for the HC method, C_{LOW} and C_{HIGH} assume similar activities.

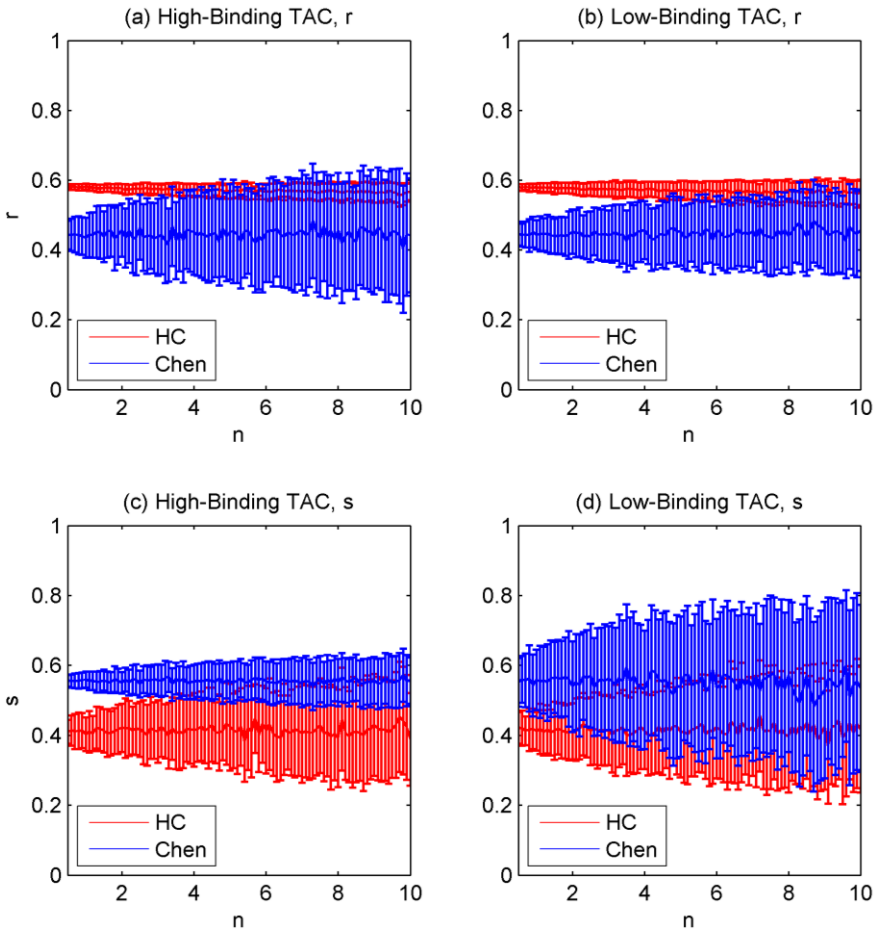

Figure 4.6 – Average and standard deviation of the correction coefficients r and s determined using the blood-based Chen's method (blue) and the blood-free HC method (red) during the PVE correction made while extracting the IDIFs from the phantoms generated in the simulation of figure 4.5.

Considering Chen's method, although the averaged values of the coefficients don't vary much when comparing both tissues, they do vary in standard deviation. The standard deviation is higher for r when using the C_{HIGH} tissue curve than when using the C_{LOW} tissue curve. At the same time, the standard deviation is higher for s when using the C_{LOW} tissue curve than when using the C_{HIGH} tissue curve. These differences in the standard deviation across different tissue curves for Chen's method are probably related to the different activities between C_{LOW} and C_{HIGH} in the late frames, see figure 4.3.

The HC method tended to overestimate r and underestimate s, when compared to Chen's method. This can be interpreted as the measured VOI values of the HC method being closer to the assumed true value (the hottest voxel) than the measured VOI values of Chen's method. One possible reason is because the assumed real values for the HC method (the hottest voxel) being values already affected by PVE, making the

average VOI values closer to the real estimates, what in turn lead to the underestimation of 20% related above.

Figure 4.7 represents how the blood-free methods vary with the number of slices considered to build the VOI of the carotid, which range from using just one slice to using five. In this particular simulation, the C_{LOW} tissue curve was used for the voxels surrounding the carotid. The HC method seems to be more robust than the H4V method to variations in the number of slices used. When diminishing that number, both the peak error and the tail error rise considerably for the H4V method, while keeping approximately constant for the HC method.

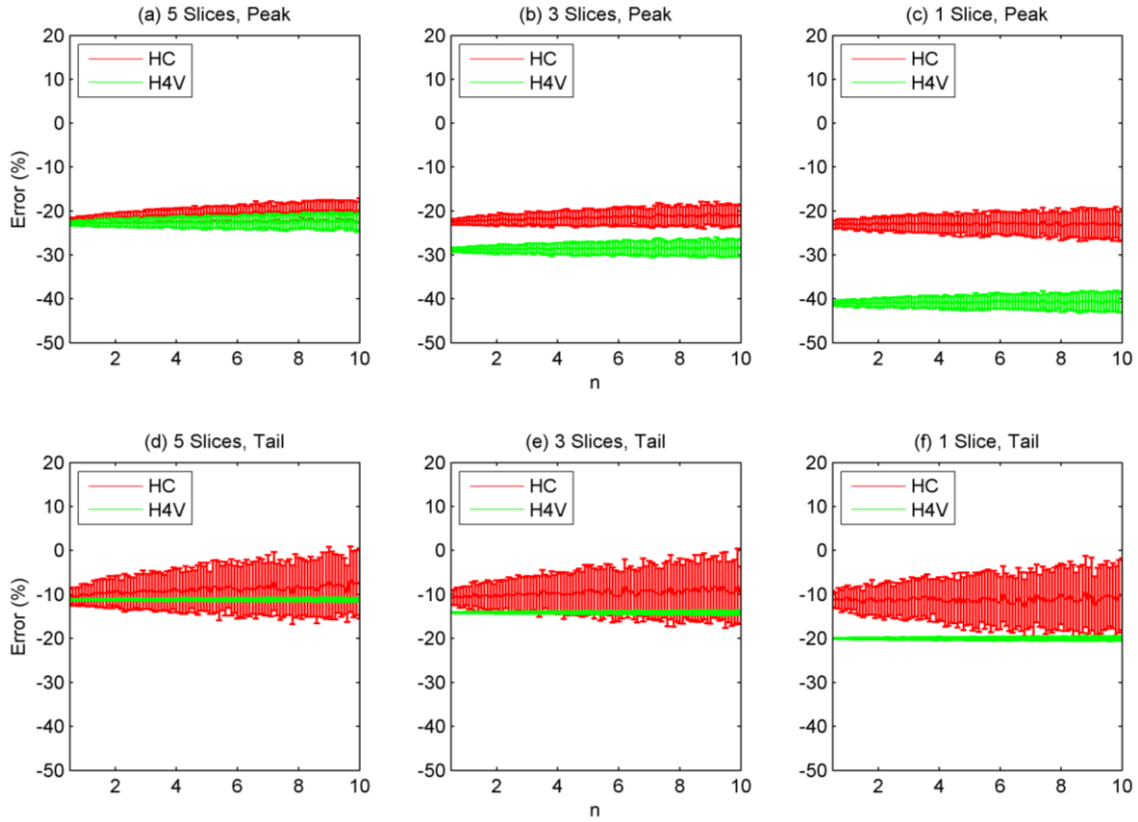

Figure 4.7 – Average error and standard deviation of the extracted TACs for 100 phantoms as function of the noise parameter n, for the blood-free HC method (red) and H4V method (green), considering the variation of the number of slices used in the carotid VOI. In this simulation, the C_{LOW} tissue curve was used to fill the voxels around the carotid.

Another parameter tested was the size of the ROI drawn in each slice of the VOI, i.e., the number of voxels included in the ROI. We observed that varying the ROI diameter between realistic values didn't significantly affect the results obtained by the blood-free methods. In fact, independently of the (realistic) number of voxels included

in the ROI, the errors obtained were qualitatively well illustrated by the plots in figure 4.5.

Finally, figure 4.8 represents the results of the comparison between Chen's method (blue) and the new suggested approach we had called the Weights method (red). The latter produces errors that are within a more narrow range of values, for all the situations, than the former. As expected, both methods produce very good results for the tail definition. In the peak definiton, the Weights method has tendency to slightly underestimate the values, but it is more robust to error variation and displays a lower standard deviation.

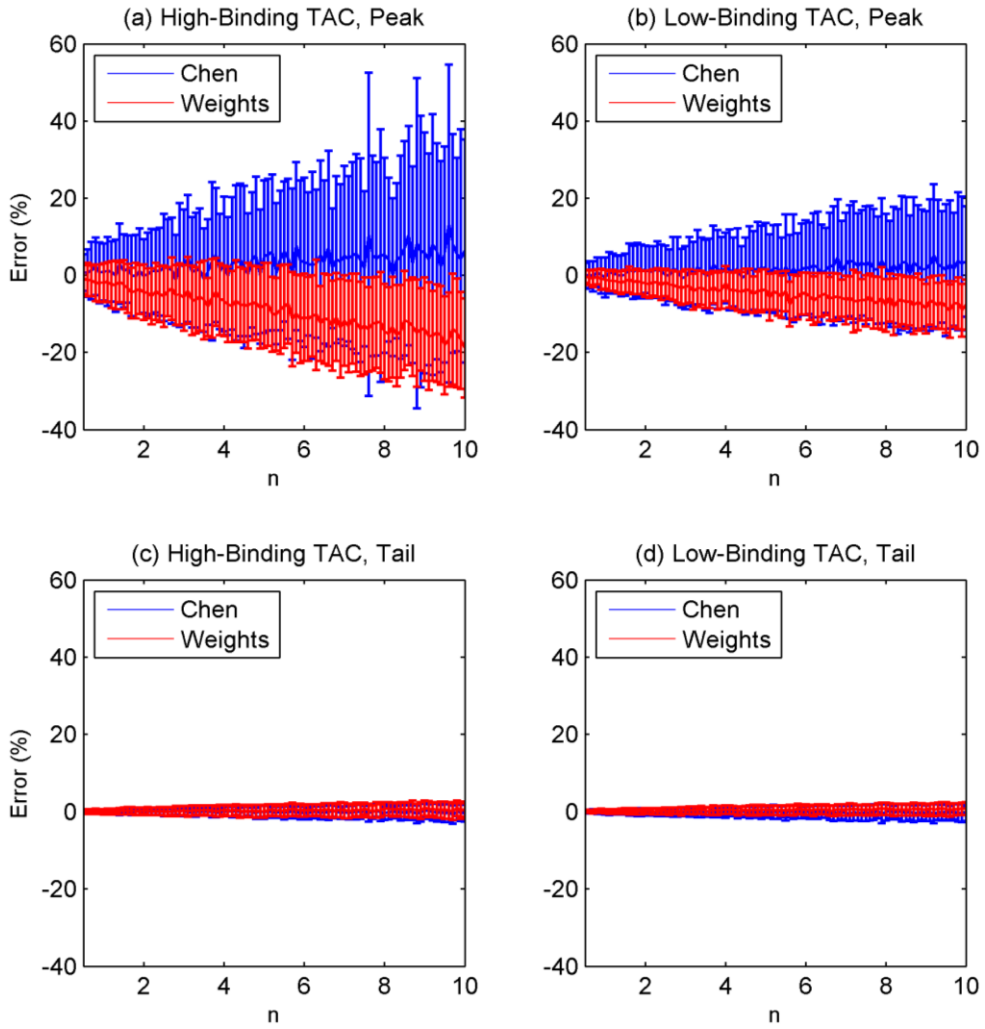

Figure 4.8 – Average error and standard deviation of the extracted TACs for 100 phantoms as function of the noise parameter n, for the blood-based Chen's method (blue) and the proposed Weights method (red). Plot (a) concerns the extracted TACs' peak error and (c) the TACs' tail error when using the C_{HIGH} tissue curve to fill the voxels around the carotid; Plot (b) concerns the extracted TACs' peak error and (d) the TACs' tail error when using the C_{LOW} tissue curve to fill the voxels around the carotid.

4.4. Discussion

This study, though quite simple, allowed questioning many different topics about the IDIF extraction methods considered.

The simulation demonstrated the efficacy of Chen's method and the clear advantage of using blood samples to calibrate the curve extracted. It is noteworthy that this method is more prone to error in the IDIF peak definition rather than in the tail. This is likely due to the fact that it uses late blood samples to derive the considered time-invariant correction coefficients. On a clinical test, (Zanotti-Fregonara, Fadaili, et al. 2009) obtained IDIFs with underestimated peak maximums and a good tail estimation using Chen's method, when comparing to curves obtained by arterial sampling.

On the other hand, blood-free methods showed a lower standard deviation than Chen's. However they underestimated the peak in about 20%, as seen in figures 4.5(a) and 4.5(b). Underestimated values were expected for the peak using blood-free methods because both of them rely on spill-out affected early image data. When considering the tail, there is also a tendency for underestimation for when low-binding tissue was considered, as seen in figure 4.5(d), but a very different performance was obtained for high-binding tissue with highly overestimated results observed, as seen in figure 4.5(c). This result illustrates how different surrounding tissues can affect the performance of the IDIF methods and how the correction coefficients work. For the H4V method, which does not depend on any PVE correction, the overestimated results at the tail may indicate that the voxels selected were very affected by the surrounding high-binding tissue. In the case of the HC, the values are not only overestimated, as also the dispersion is high. As the HC method derives the PVE correction coefficients using the hottest voxel from inside the carotid region for three peak-coincident frames for calibration purposes, the outcome coefficients will better characterize how the extracted data is affected by tissue in the early time-frames. In the early frames, there is a spill-out tendency, since the carotid's C_B curve assumes high activity values when compared to the surrounding tissue, see figure 4.3. In the case where we consider high-binding tissue, in the late time-frames the C_{HIGH} curve assumes higher activity values than the C_B curve. This means that extracted carotid TAC will be affected in a spill-in way, the opposite to what happens in the peak-coincident frames. All this associated with the fact of using compromised image data for calibration purposes leads to the results shown.

In the study (Zanotti-Fregonara, Fadaili, et al. 2009) a comparison is established between several IDIF extraction methods, by simulating them in a phantom and applying them to [^{18}F]-FDG images. Interestingly, in the simulation of the method proposed by (Su et al. 2005), the results shown a tendency for underestimation of the peak and overestimation of the tail - the area under the curve at the tail region is overestimated by 33.6%. This result is similar to the result found in the present phantom study using the HC, which uses a PVE correction similar to that used in (Su et al. 2005). (Zanotti-Fregonara, Fadaili, et al. 2009) confirmed that the overestimation of the tails happens most likely due to an underestimation of the tissue spillover into the carotids, because of the lower uptake by brain tissue at the early frames of the PET exam, where the correction coefficients are derived from, just as explained above.

The average errors obtained using Chen's method to estimate the peak region are similar, despite of the binding level of the surrounding tissue. However, there is less variability when low-binding tissue is considered, see figure 4.5(b). This is consistent with the fact that the correction coefficients were estimated using late blood samples, and therefore will reflect the spill-in tendency on the late frames when the high-binding tissue curve was used.

The results obtained when using low-binding tissue are in general better for all methods. As seen in figure 4.3, in late time-frames the C_{LOW} tissue curve has lower values than the blood curve, inducing spill-out, likewise with what happens in early-frames. As a result, for both blood-free methods and Chen's method better performance is achieved.

Focusing on comparing the blood-free methods between each other, the HC method demonstrated to have slightly better performance than the H4V method, except for the tail in the situation of using the C_{HIGH} tissue, which can be explained considering how the HC method depends on the calculation of the correction coefficients. By diminishing the number of slices used in the carotid VOI, the H4V method performance decreased significantly both for the peak and tail estimation, whereas the HC method remained approximately constant, proving to be more robust to this variation. This result suggests that the H4V method strongly relies on information given from different slices. Considering a VOI that includes 5 slices, the four hottest voxels would most likely belong to different slices, each one corresponding to the hottest of the slice. Decreasing the VOI to one slice, the method will consider the four hottest voxels of the ROI uniquely from that slice, introducing lower-value voxels more affected by PVE. On

another test, varying the ROI size in each slice did not significantly affect the performance of any of the methods probably because the hottest voxels considered didn't change.

The Weights method produced absolute errors deviating in average from zero more than Chen's method, but the dispersion of the results was considerably inferior and the method was robust to noise variation. In opposition to Chen's method, the Weights method showed tendency to slightly underestimate the results. In general, it may be considered a promising approach, mostly due to the way the correction coefficient constants are calculated. In the traditional Chen's PVE correction, the r and s values are calculated considering an average of several voxels from each carotid ROI. In the Weights method, the PVE correction is made for each voxel of the carotid ROI zone individually. It makes a partial volume correction by calculating how each voxel within the carotid region contributes to the real blood concentration value. It is equal to perform the calculation of the r coefficient alone for each voxel, and for this reason no tissue input is required. In the end, the Weights method calculated matrix represents each voxel contribution for the real value of the function. This way, a more specific PVE correction is made and this is probably the reason why the Weights method performs better to estimate peak values in the sense that Chen's method's variability may lead to more aberrant results.

4.5. Conclusion

This study assesses the different performances of blood-free methods and blood-based ones. Looking back to the results of this simulation, it is suggested that blood-free methods provide underestimated IDIFs.

The HC method, when applied to the phantom we suggested, displays a more accurate and robust performance. It is also suggested that considering the hottest voxel as being less affected by PVE estimation and then as a good estimation for the real C_B value may be a good assumption, although possibly noisy.

Considering this, one may think a good approach may be doing exactly the same than in H4V method but considering only a single voxel, the hottest one, instead of four. However a single voxel to extract the function per frame should be very exposed to noise in the later frames. This highlights the advantages of the HC method. It uses the

hottest voxel in a zone where the C_B function is highly distinguishable from the surrounding tissue (in the peak) and derives the coefficients that can be applied in later times. Although the tail seems to be very challenging to obtain in the high-binding tissue situation, when considering real data the surrounding tissue should not take such high values. The receptor-rich region of the [^{11}C]-Raclopride (the striatum) is in a higher area of the head than the area where the carotids VOI selection should be made (below the Circle of Willis). The test was performed in this simulation to evaluate different situations and better understand the role of this variable in the method's efficacy. It is more realistic, in this sense, to consider the results with low-binding tissue.

All together this simulation suggests that despite the differences between using or not blood samples to calibrate the extracted TAC, the best non-invasive approach for using in the next chapter should be the HC method.

5. IDIF Extraction and Quantification of [^{11}C]-Raclopride PET Images

5.1. Introduction

This chapter concerns a totally non-invasive IDIF study using [^{11}C]-Raclopride PET images. The blood-free IDIF methods introduced in the previous chapter were used to derive the AIF and determine the binding potential distribution for a group of subjects.

The initial bibliography research about IDIF techniques strongly suggested that blood samples, even in a reduced number, are important to correct for PVE and to estimate the amount of metabolites and the plasma fraction. Ideally, this study would dispose of a blood-sampling procedure for a more accurate study, but such was not possible. As a solution, the IDIF methods applied relied on the assumption that a number of hottest voxels from inside the carotids VOI were less affected by PVE, as studied in the previous chapter. In addition, the correction for metabolites and the determination of the plasma fraction was made using data from the literature.

In the lack of a gold-standard AIF determined using arterial sampling to assess the results of the IDIFs extracted, the IDIFs were used as input in the estimation of the binding potential, and the results were compared with binding potential values determined using a validated alternative method for [^{11}C]-Raclopride, the SRTM, as mentioned in chapter 2.

5.2. Materials

[^{11}C]-Raclopride] PET images were obtained from ongoing patient studies, in ICNAS, involving healthy volunteers and patients with Parkinson's Disease. The PET images were obtained using a Philips Gemini GXL 16 scanner, 2009 model. The total scanning time was 90 minutes. The data was reconstructed using a LOR-

RAMLA algorithm, the framing sequence being 4 x 15 s, 4 x 30 s, 3 x 60 s, 2 x 120 s, 5 x 240 s and 12 x 300 s, and corrected for motion effects on SPM8. The data was later quantified using SRTM and employing the cerebellum as the reference region.

All the analysis presented in this chapter were made using Matlab (The Mathworks, Inc., USA), which include simulations, IDIF method's implementation (including raw-TAC extraction, PVE correction and metabolite and plasma fraction correction) and statistical calculations.

5.3. Methods

5.3.1. Evaluating IDIF Performance Using the Binding Potential

In this study, since there is not any blood sampling procedure, it is not possible to produce a gold-standard arterial input function, extracted through arterial sampling, to directly compare the IDIFs determined and evaluate the efficacy of the IDIF methods.

To overcome this problem, IDIFs were not directly compared to any curve. Instead, the figure of interest was rather the binding potential. To obtain this, the IDIFs extracted were used as inputs to compartmental models. This allowed determining the binding potential both for a VOI of the striatum, which is the high-binding region for [^{11}C]-Raclopride, and voxel-wise – generating parametric images. The binding potential values determined using the IDIFs were compared to a verified solution: the binding potential generated using a validated method as an alternative to the gold-standard: the Simplified Reference Tissue Model. The latter resorts to a compartmental model that uses as input the TAC of a reference region, which is, for [^{11}C]-Raclopride, the cerebellum, as studied in chapter 2.

The quantification performed using IDIF as the input for the models was made through two different quantification methods: the two-tissue compartmental model and the Logan plot.

As mentioned in chapter 2, by solving the two-tissue model is possible to estimate the kinetic parameters K_1, k_2, k_3 and k_4, from where the binding potential is derived as k_3/k_4. This model can be described by the equations 2.2, 2.3 and 2.5. To solve those equations, a linear least squares method was used, based on the work of (Cai et al. 2002):

$$C_{PET}(t) = P_1 C_B(t) + P_2 \int_0^t C_P(\tau)d\tau + P_3 \iint_{0\,0}^{t\,\tau} C_P(s)dsd\tau + P_4 \int_0^t C_{PET}(\tau)d\tau + P_5 \iint_{0\,0}^{t\,\tau} C_{PET}(s)dsd\tau \quad (5.1)$$

This model has in consideration the volume of blood V_B, which in the above equation 5.1 takes the form of P_1. As for C_B, it corresponds to the whole-blood PVE-corrected curve extracted, C_P corresponds to the metabolite-corrected plasma curve and C_{PET} corresponds to the TAC of the voxel or ROI we want to quantify. By solving this multi-linear equation with linear least squares it is possible to derive the coefficients P_1 to P_5, from which the target parameters were finally derived as follows:

$$V_B = P_1 \quad (5.2)$$

$$K_1 = \frac{P_1 P_4 + P_2}{1 - P_1} \quad (5.3)$$

$$K_2 = -\frac{P_1 P_5 + P_3}{P_1 P_4 + P_2} - P_4 \quad (5.4)$$

$$k_3 = -(k_2 + k_4 + P_4) \quad (5.5)$$

$$k_4 = \frac{-P_5}{k_2} \quad (5.6)$$

This approach has the advantages of providing a fast solution and being able to be solved in one step. For the least squares method, upper and lower bounds were established for each of the coefficients P_1 to P_5 by assuming biologically plausible intervals of the values of the kinetic constants K_1, k_2, k_3 and k_4. The blood volume V_B was considered to be invariant and equal to 4%, according to (Leenders et al. 1990).

The other quantification method used was the Logan plot. This allows estimating the distribution volume (DV) of a region, using the arterial plasma function as input, through equation 2.9. After a certain time *t*, this equation becomes linear and the DV

can be extracted from the slope. The DV of a high-binding region, which for [^{11}C]-Raclopride corresponds to the striatum, is equal to

$$DV_{HIGH} = \frac{K_1}{k_2}\left(1 + \frac{k_3}{k_4}\right) \quad 5.7$$

and can be determined through equation 2.14 using as input the plasma metabolite-corrected input function and the TAC of the VOI or voxel of the high-binding zone. The DV of a low-binding zone (reference region), as it is devoid of receptor sites, is simply given by

$$DV_{LOW} = \frac{K_1'}{k_2'} \quad 5.8$$

and can be determined through equation 2.14 using as input the plasma-metabolite corrected input function and the TAC of a VOI of the reference region, which is for [^{11}C]-Raclopride the cerebellum. By assuming the ratio of the transport constants K_1/k_2 to be the same on both the high-binding zone and the low-binding zone (the same assumption is made in the reference tissue model) the binding potential can be estimated as

$$BP = \frac{k_3}{k_4} = \frac{\frac{K_1}{k_2}\left(1 + \frac{k_3}{k_4}\right)}{\frac{K_1'}{k_2'}} - 1 = \frac{DV_{HIGH}}{DV_{LOW}} - 1 \quad (5.9)$$

By using the Logan plot this way, although the input function is the IDIF, we indirectly need a reference region TAC to determine the binding potential of the striatum, unlike using the two-tissue compartmental model, which requires only the arterial concentration. Nevertheless, this method was chosen in addition to the two-tissue model because of how IDIF errors affect the DV values calculated and, in the end, the binding potential. Therefore, the Logan plot was used as an additional tool to better understand the differences between the IDIF methods and the type of errors that are being committed.

Finally, the gold-standard BP values of the VOIs from the striatum were determined using the SRTM by solving equation 2.13, introducing the reference region TAC as input and the TAC of the VOI we wanted to quantify. For the voxel-wise

quantification, we used the approach proposed by (Gunn et al. 1997), which linearizes the operating equation of the SRTM, thus providing a faster approach less sensitive to noise.

5.3.2. Comparison Between the Quantification Models Used

The binding potential values determined by different quantification models may have some variability. It is important to verify what is the expected difference between the BP values determined with the three quantification methods used in this chapter.

To evaluate that difference, perfect curves were generated through the same process used in chapter 4 and fitted to the models. We used the same [^{11}C]-Raclopride plasma metabolite-corrected curve extracted from (Farde & Halldin 1989), the same kinetic constants and equations 4.2, 2.2, 2.3, 2.5, 4.3 and 4.4 to generate C_B, C_T and C_R.

To introduce variability in the curves, the several parameters of the C_P curve in equation 4.1 were multiplied by a random number between 0.5 and 1.5, this way generating C_P curves with different shapes. Holding the kinetic constants invariable, the calculated C_T and C_R for each variation of C_P would also have some variability but still perfectly fit the models. For each variation, as the kinetic constants were always the same, one should always obtain the same BP.

For each combination of C_P and resulting generated curves C_B, C_T and C_R, the binding potential was determined using SRTM, Logan plot and the two-tissue model and finally compared.

5.3.3. Understanding How IDIF Errors are Processed by the Two-tissue Model and by the Logan Plot

A clear disadvantage of not having a gold-standard AIF is not being able to identify the errors that are being committed in the IDIF extraction. Relying on the quantification parameters BP and DV to understand the errors associated to the IDIF extraction implies in first place understanding how those parameters should vary with regard to the expected IDIF errors.

To determine the relationship between variations on the AIF and the resulting quantification parameters, a simulation was made. In that simulation, on one side, we used invariant C_T and C_R curves, so that the quantification parameters should remain

constant. On the other hand, several variations of the C_P curve were performed by varying its parameters in equation 4.1, this way achieving C_P curves with different peaks and tails. We observed how the BP and the DV values changed as a function of the overestimation and underestimation of the peak and tail regions of the C_P curve.

5.3.4. IDIF Determination

In this subsection, we will describe how IDIFs were extracted. Two methods were considered: the HC method and the H4V method, both studied in the previous chapter.

5.3.4.1. Whole-Blood TAC Extraction and PVE Correction

The methods did not substantially vary from the description made in the previous chapter. Nevertheless, a more detailed description is made below.

In first place, the carotids VOI selection was made. The first 5 frames were summed (frames that cover the function peak) and the carotid arteries segmentation was made in the resulting image. The number of summed frames was sometimes adjusted for a better identification of the arteries. The selection was made manually, using a drawing tool, since is simpler to implement, efficient and totally controllable.

A ROI was drawn for each carotid on several slices, corresponding to the ones that captured the portion of the cervical segment of the carotids (see figure 4.1). In that zone, they are well-defined and the voxels are less affected by spill-in activity from the brain. The ROIs were manually drawn for groups of 3 to 6 slices. The number of slices was adjusted according to changes in the carotid definition on the image.

The total VOI determined was common to both the HC and the H4V methods. The differences between the methods start after the carotid VOI selection.

First, we'll analyze the HC method. Using the total carotids VOI determined, consisting of several voxels from several slices, a mask was derived. That mask was multiplied by all frames. The TACs of each voxel of the mask were averaged, computing the whole-blood raw-TAC. At the same time, a TAC of the tissue surrounding the carotids was determined. That TAC was derived by placing a comma-shaped ROI in a region close but not adjacent to each carotid artery ROI. Then, the PVE correction was made, according to the model proposed by (Chen et al. 1998), specified

in equation 3.1. In that equation, the real values of the input function were approximated by the hottest voxel found inside the carotid VOI for three early frames whose times matched the function peak. Using the tissue-TAC values and the whole-blood raw-TAC values for those frames, the correction coefficients r and s were derived using linear least squares. By assuming the correction coefficients were invariant in time, the whole-blood raw-TAC was corrected for all frames, according to equation 3.2, leading to the whole-blood PVE-corrected curve.

For the H4V method, the differences when compared to the HC method relies in the mask elaborated and in the fact that no PVE correction was made. From the same carotids VOI extracted using the summed early frames, a mask was built containing the four hottest voxels of the whole carotid VOI. That mask, containing four voxels, was then multiplied by all frames. The TACs of the four voxels were averaged, yielding the whole-blood PVE-corrected curve, because we assumed that those four voxels would be free of PVE.

5.3.4.2. Fitting, Correction for Metabolites and Plasma Fraction Calculation

In order to obtain the final plasma metabolite-corrected input function the whole-blood PVE-corrected curves extracted using both methods were fitted with an exponential model and corrected for metabolites and plasma fraction, generating the final IDIF curve.

For each method, the whole-blood PVE-corrected curve was fitted with the same 3-exponential model used in chapter 4, described by equation 4.1. The main interest of this step is the reduction of measurement noise.

The correction for metabolites and accounting for the plasma fraction was based on the work done in the previous chapter. The difference is that then, to assign the phantom a whole-blood curve, a conversion was made from the plasma curve C_P to the whole-blood curve C_B. Now the opposite is required, following the same steps but in the opposite order. The whole-blood PVE-corrected TACs extracted from the PET images represent both the unchanged radioligand and its metabolites in blood. One wants to isolate the unchanged parent concentrated in plasma.

The metabolite correction was done using the same parent fraction curve introduced in chapter 2, represented in figure 2.7. Finally, the plasma concentration of

the tracer was determined assuming the relation 2.19 and approximating *HCT* by 0.5. Joining equations 2.18 and 2.19 together, the final IDIF was computed as follows:

$$IDIF(t) = \frac{C_B(t)}{(1 - HCT)} \times ParentFraction(t) \tag{5.10}$$

where C_B is the whole-blood PVE corrected curve, *HCT* the hematocrit, *ParentFraction* the curve represented in figure 2.7 and IDIF the final plasma metabolite-corrected arterial input function derived from the PET image.

5.3.5 Assessing the Accuracy of the IDIFs

For each subject, an image-derived input function was extracted from the internal carotid arteries. A tissue TAC from the cerebellum (the reference region for Raclopride) using a cerebellum mask was additionally obtained.

As a first test, the BP was determined for a TAC extracted from a VOI of 20 voxels of the striatum, which is the high-binding zone for [^{11}C]-Raclopride.

The BP was determined using the two-tissue compartmental model and the Logan plot and the results were compared to the reference solution obtained using SRTM. The two-tissue compartmental model was solved according to equation 5.1, by introducing as input the IDIF, the corresponding whole-blood PVE-corrected curve (to determine V_B) and the TAC of the striatum VOI. The BP was finally determined as being k_3/k_4. Additionally, another approximation for BP was also determined using the Logan plot by computing DV_{HIGH} using the IDIF and the TAC of the striatum VOI, by determining DV_{LOW} using the IDIF and the reference region TAC, and finally applying equation 5.9 to determine the BP. On the other side, the reference BP was determined with the SRTM using the reference tissue curve as input and the TAC of the striatum VOI.

As a second test, we performed the same approach described above to compute parametric images displaying the BP. The only difference is that instead of the TAC extracted from the VOI of the striatum, one has to consider the TAC of each voxel, to produce the BP for each voxel.

5.4. Results

In this section, we will first evaluate what is the expected difference for the BP determined by the several models and how the quantification parameters vary as function of the IDIF errors.

Secondly, the results of the IDIF extraction, the quantification of the striatum VOI and the generation of parametric images will be evaluated.

5.4.1. Comparison Between Quantification Models

By fitting several variations of the perfect curves to the models, it was possible to observe the resulting difference of calculating BP using the two-tissue model and the Logan Plot relatively to the BP calculated by the widely used SRTM. The BP values estimated by fitting the curves with the two-tissue model were shown to have an overestimation of 6% in comparison to the BP determined using SRTM. On the other hand, the BP values estimated using the Logan Plot were very close to the ones estimated with SRTM, with a small difference of less than 1%.

5.4.2. How the Two-Tissue Model and the Logan Plot Process IDIF Errors

A total of 2000 variations of the perfect curve C_P were generated by multiplying the corresponding parameters by a random number between 0.8 and 1.2. In the first place, we tested the two-tissue model. Using an invariable C_T curve, corresponding to a high-binding curve, each generated C_P was taken as input to generate the BP with the two-tissue model. We separately evaluated how the peak variation and the tail variation of C_P affected the BP. The peak error was measured as the relative difference between the maximum of the modified C_P and the maximum of the perfect C_P. The tail error was taken as the average relative difference between the modified C_P and the perfect C_P, measured between t=700 and t=5400 seconds. The BP errors were measured as the relative difference of the BP generated using the modified C_P and BP generated using the perfect C_P.

In figure 5.1 the results for the two-tissue model are represented. On the left, figure 5.1 (a) is a plot of the BP error as a function of the peak error. For this plot, only data corresponding to a tail error between -5% and 5% was considered. It is possible to

notice a high sensitivity to peak variation, inducing a large dispersion of the BP values. It is possible though to observe a tendency to overestimate the BP values when there is an underestimation of the peak and an underestimation of the BP values with an overestimation of the peak. On the right, figure 5.1 (b) represents a plot of the BP error as function of the tail error of C_P. Similarly to the previous plot, in this one only data corresponding to a peak error between -5% and 5% was considered. In this analysis, besides the dispersion of the results, there is a clear tendency to overestimate the BP values with an underestimation of the tail.

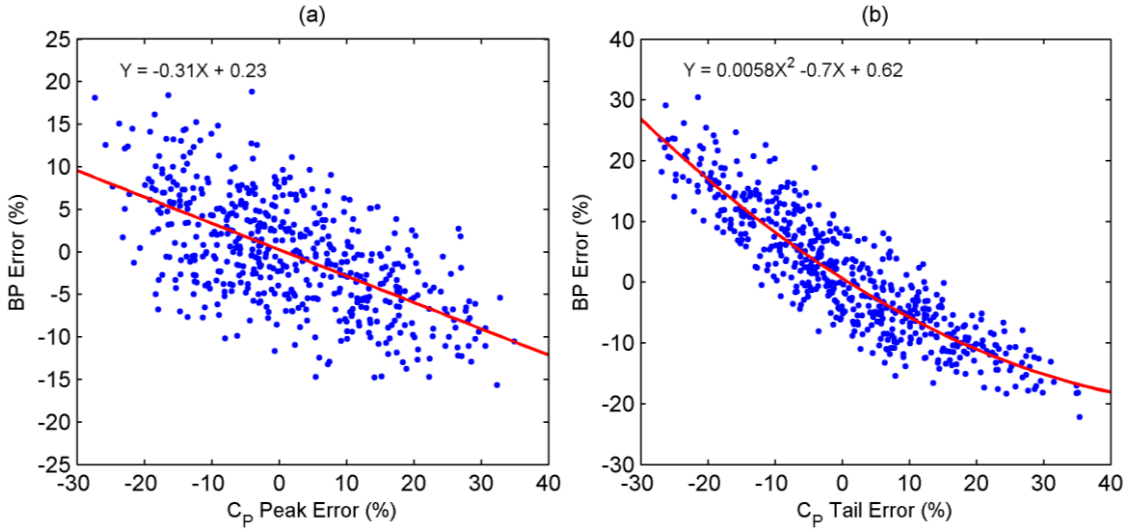

Figure 5.1 – Error of the BP estimated using the two-tissue compartmental model as function of the peak (a) and tail (b) error of the C_P.

In the second place, we tested the Logan plot. Using each variation of C_P, the same invariant C_T and an invariant C_R corresponding to a low-binding tissue curve, DV_{HIGH} and DV_{LOW} values were generated, respectively, and finally BP was derived according to 5.9. The Logan plot takes as input coordinate points corresponding to latter time frames. Therefore, for this method the tail of the IDIF is the most important source of error in the estimation of the DV and BP. Similarly to what was done above, for this test the BP and DV errors were measured as the relative difference between the BP and DV generated using the modified C_P and BP and DV generated using the perfect C_P.

In figure 5.2 (a) the DV_{HIGH} error as function of the peak error is represented. Similar results were found for the DV_{LOW}. Similarly to above, only the data with a tail error between -5% and 5% was considered. It is possible to observe a high dispersion of the DV_{HIGH} error, with a slight tendency to overestimate DV_{HIGH} with an underestimation of the peak of C_P. On the contrary, as expected, a very clear tendency

was found by considering the tail error. Figure 5.2 (b) is a plot of the DV_{HIGH} error as function of the tail error, for data in which the peak error varied between -5% and 5%. It clearly demonstrates the sensitivity of the method to IDIF tail errors in estimation of DV.

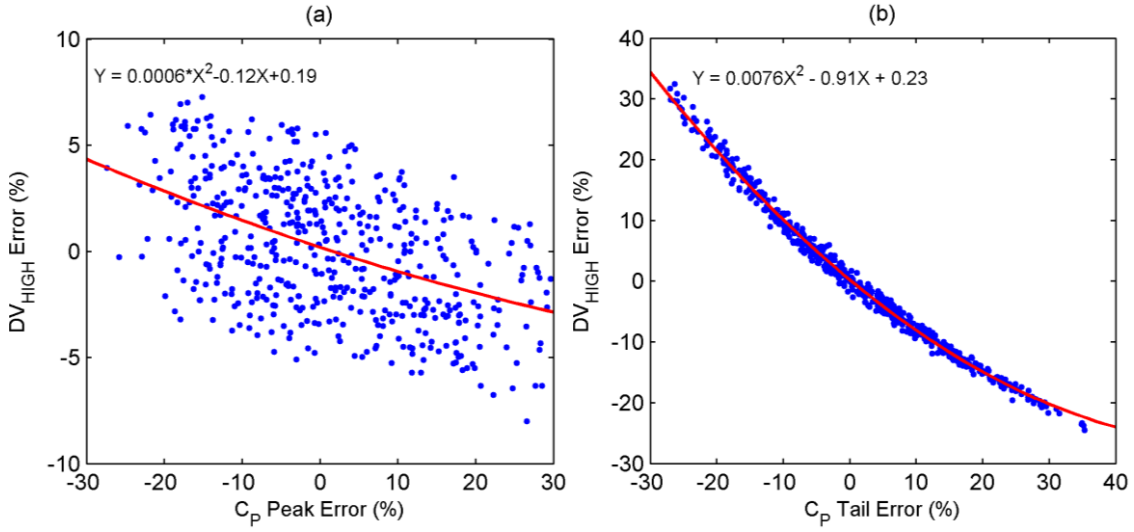

Figure 5.2 – Error of the DV_{HIGH} estimated using the Logan plot as function of the peak (a) and tail (b) error of the C_P.

Finally, a relationship was sought between the BP determined using the Logan plot and the error in the tail. Figure 5.3 is a plot of the BP error as function of the tail error of the C_P curve. It is possible to observe, in contradiction to the two-tissue compartmental model, a tendency to underestimate the BP with an underestimation of the tail. The BP error variation is, however, lower than the BP error for the tail using the two-tissue model, see figure 5.1 (b). This means that the Logan plot is more robust to errors in the tail of the AIF than the two-tissue model. This is probably due to the fact that the BP determined with the Logan plot is a result of a ratio between DV_{HIGH} and DV_{LOW}, which are affected by the IDIF errors in the same manner.

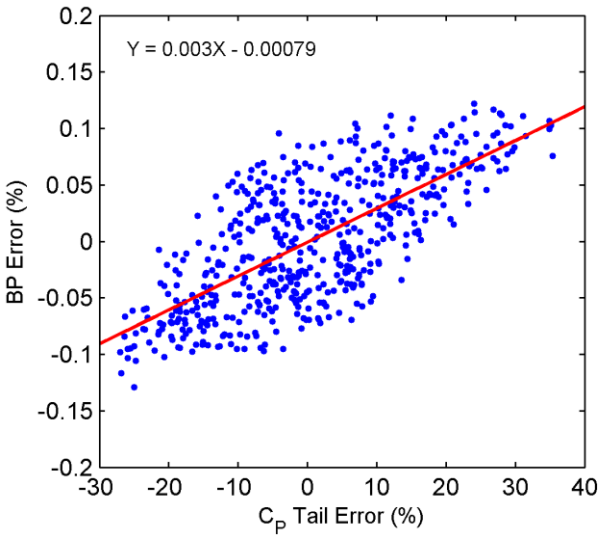

Figure 5.3 – Error of the BP estimated using the Logan plot as function of the tail error of the C_P.

5.4.3. Extraction of IDIFs

In this subsection we'll analyze several topics on the IDIF extraction process made.

In the carotid ROI selection, there were some hotspots that mislead the identification. Some of those hotspots correspond to other blood vessels, as for example the vertebral artery or the external carotid artery. The best way to locate the internal carotid arteries, which are the ones that provide arterial blood to the brain, consisted in watching a slice sequence and observing hotspots changes accordingly to the predicted carotid shape. A reference point is certainly the Petrous section of the carotid. In this section, the carotid curves anteriorly and medially, and that curve is easy to identify, because it adopts a more distinct and identifiable shape from the entire resulting tracer pools. The slices for IDIF extraction were selected to belong to the section previous to the Petrous segment, which is named the Cervical segment, to avoid spill-in activity from the brain. In the upper slices, after the Petrous section, hotspots that corresponded to the carotids region were found. Some tests were made and the values extracted were found to be higher than the values of the IDIFs that produced good BP agreement, suggesting the values were overvalued by spill-in effects. With no samples available to

calibrate the extracted data, all efforts should be done to seek for the less affected voxels.

After summing the first five frames, the range of the resulting image was set between zero and the maximum value of the whole summed image, attenuating undesired hotspots and enhancing the carotids. This was done, in the first place, to identify the carotids. Once identified, the range for the visualization of each slice was set between zero and the maximum of the slice, for achieving a better definition.

For a given image, the best results after quantification were found to be associated to regions of interest containing small, well defined carotid areas in which a good contrast is found between the carotids ROI and the surrounding tissue, see figure 5.4 (a). There are identifiable carotid areas that are surrounded by high valued tracer pools, and this was an indicator for compromised spill-in affected values, see figure 5.4(b).

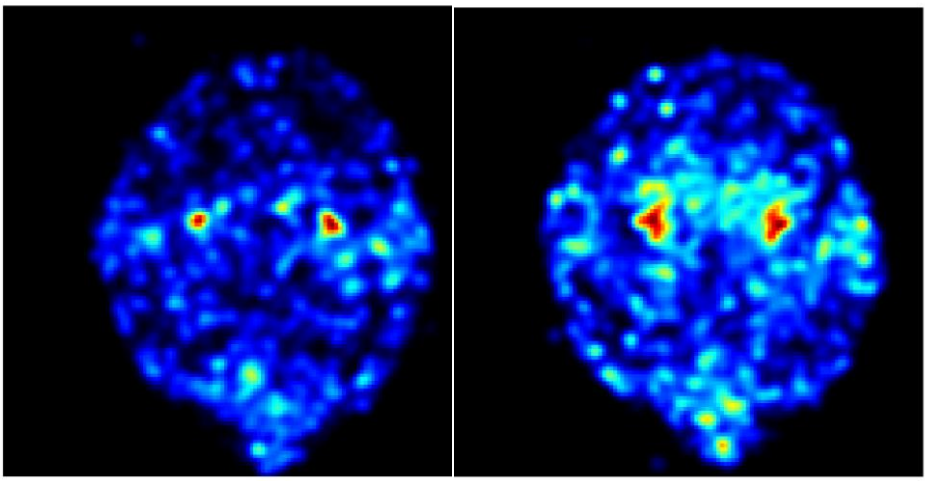

Figure 5.4 – Example of different situations found when defining the carotids ROI. On the left, the carotids, corresponding to the red circular zones, are smaller and better defined than in the image of the right.

Focusing on the performance of the different IDIF methods, the H4V method had a tendency to produce IDIF curves with lower values than the HC method. For all subjects there was an underestimation of the peak using the H4V method, on average -14.4±11.23 %, when compared to the HC method. There was also an underestimation of the tail for 85% of the subjects, on average -43.70±8.93 % tail value, when compared to the HC method.

For each subject it was evaluated if the surrounding tissue assumed higher values than the average values of the carotid VOI for later frames, in order to exclude the situation of overestimation of the tail values, as studied in the previous chapter. The relative difference between the averaged voxels of the carotid VOI and the averaged voxels of the surrounding tissue VOI was, for later frames, always positive, giving an average of +28.31±12.38%.

In figure 5.5 the several curves determined in the IDIF extraction process for one subject are represented as an example.

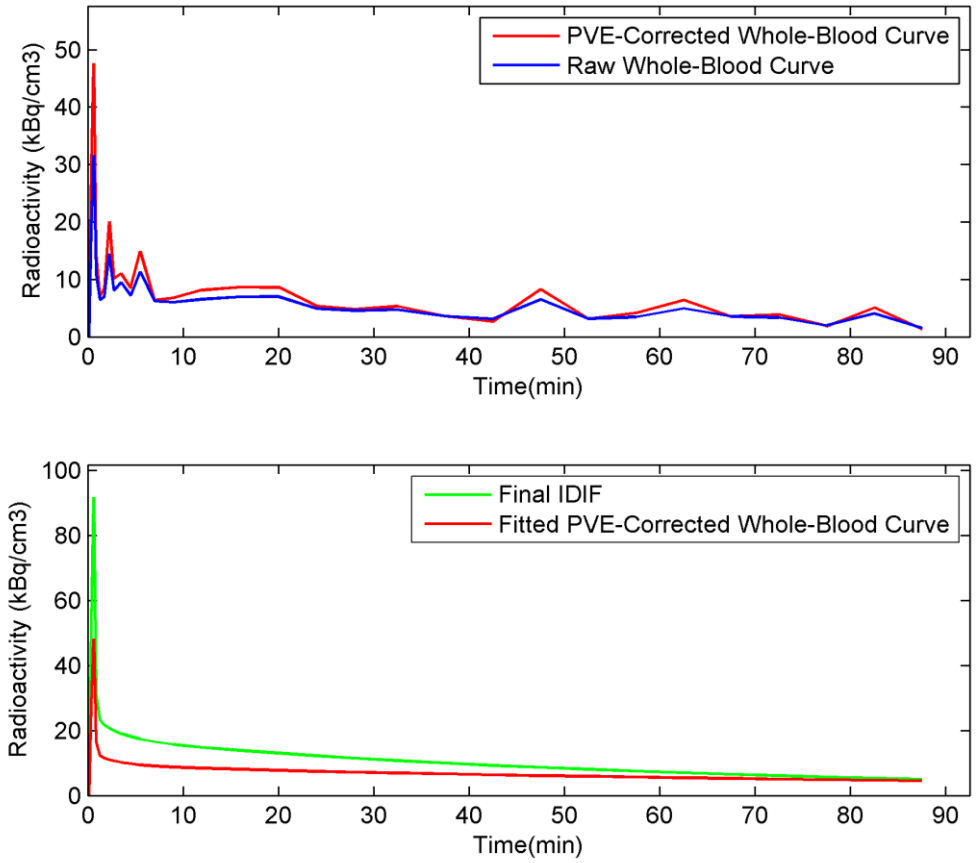

Figure 5.5 – All the curves derived throughout the IDIF extraction process using the HC method, for one subject. The raw curve extracted from averaging the carotids VOI voxels' TACs (top-blue). The corresponding PVE-corrected curve, after determining the correction coefficients (top-red). The fitted PVE-corrected whole-blood curve (bottom-red). And finally, after correcting for metabolites and plasma fraction, the IDIF curve (bottom-green).

5.4.4. Determining the BP Using a Striatum VOI

Before calculating the parametric images, the BP was generated for a VOI of 20 voxels of the striatum for each subject, using both the two-tissue compartmental model and the Logan Plot and, in both cases, the IDIFs computed using HC and H4V as input, see Table 5.1. In this, the reference values for the BP over the striatum of each subject, computed using SRTM, are included.

Using the two-tissue compartmental model, the resulting BP values showed a high dispersion, with a tendency to be overestimated for both the HC and the H4V methods for obtaining the IDIF. Better results were achieved with the IDIFs generated by the HC method, with an average BP error of +16.55 ± 87.13%. For the case of the IDIFs determined using the H4V method the error was quite high: +97.05 ± 165.34%.

Table 5.1 – Binding potential determined for a VOI of 20 voxels of the striatum, using the validated SRTM and using the two-tissue model with the IDIFs extracted with the HC and the H4V method as input.

Subject Nº	SRTM	Two-Tissue Model	
		Hybrid Chen	Hottest4Voxels
1	3.28	2.60	7.39
2	3.60	8.33	9.89
3	2.94	6.66	10.52
4	1.95	0.43	0.48
5	4.10	1.62	1.20
6	3.40	2.48	2.01
7	2.83	2.14	5.88
8	2.98	2.30	1.78
9	2.26	6.82	9.40
10	3.67	5.16	7.86
11	3.76	3.39	3.91
12	3.04	3.99	16.49
13	3.68	0.94	1.67

Using the Logan Plot to determine the BP, significantly better results were achieved for both IDIF extraction methods, see Table 5.2. In this case, BP values were

on average underestimated by -6.92 ± 5.69% for the HC method and -6.51 ± 4.46% by the H4V method, using again the SRTM values as reference. The DV_{HIGH} values estimated by the H4V method were superior to the DV_{HIGH} values estimated by the HC method in average by +54.18 ± 46.88%. A similar result was found for DV_{LOW}: +54.43 ± 48.40%.

Table 5.2 – BP determined for a VOI of 20 voxels of the striatum, using the validated SRTM and using the Logan plot with the IDIFs extracted with the HC and the H4V method as input, by determining DV_{HIGH} and DV_{LOW}.

Subject Nº	SRTM	Logan Plot					
		Hybrid Chen			Hottest4Voxels		
	BP	DV_{HIGH}	DV_{LOW}	BP	DV_{HIGH}	DV_{LOW}	BP
1	3.28	0.91	0.22	3.12	1.96	0.48	3.06
2	3.60	1.37	0.33	3.18	2.00	0.48	3.20
3	2.94	0.69	0.19	2.60	1.03	0.28	2.70
4	1.95	0.63	0.21	1.93	1.27	0.43	1.93
5	4.10	1.42	0.29	3.83	2.44	0.52	3.72
6	3.40	1.48	0.34	3.28	2.56	0.60	3.27
7	2.83	1.31	0.35	2.75	2.91	0.77	2.76
8	2.98	1.09	0.27	2.99	1.68	0.42	2.99
9	2.26	0.88	0.28	2.17	1.41	0.46	2.10
10	3.67	2.73	0.70	2.92	2.16	0.53	3.10
11	3.76	2.00	0.44	3.55	2.53	0.56	3.56
12	3.04	2.19	0.60	2.66	1.41	0.36	2.91
13	3.68	1.19	0.27	3.46	1.65	0.38	3.29

A correlation was made between the BP values determined with the SRTM and the BP values determined with the Logan plot, for both the situations of using IDIFs extracted with the HC method and using IDIFs extracted with the H4V method, and is represented in figure 5.6.

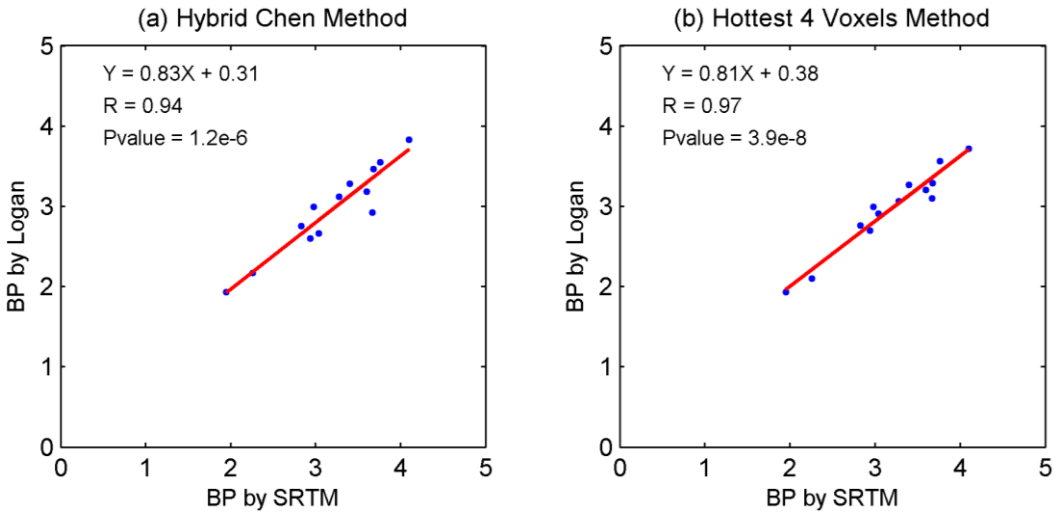

Figure 5.6 – Correlation between the BP values determined using the SRTM and the BP values determined using the Logan plot considering IDIFs extracted using the HC method (a) and the H4V method (b).

5.4.5. Voxel-Wise Quantification

Parametric images, in which the BP is determined for each voxel individually, were obtained using the two-tissue compartment model and the Logan plot, using IDIF as input function. The resulting BP parametric images generated using those methods were compared with the BP parametric images generated by the SRTM, which in turn took the reference region TAC as input.

Generating parametric images using the two-tissue compartmental model, by solving equation 5.1 for each voxel individually using the IDIF of the subject as input, was found to yield acceptable results for only 3 subjects: subject one, seven and eleven (23% of the subjects). For those three subjects, only the IDIF estimated using the HC method provided good results. In general, the parametric images determined with the two-tissue model had the tendency to overestimate the BP in each voxel.

The voxel-wise quantification was performed for each subject for one slice coincident to the zone we are particularly interested in quantifying, the striatum. In figure 5.7 the resulting parametric images for the SRTM (left) and the ones determined using the two-tissue compartmental model (right) are represented.

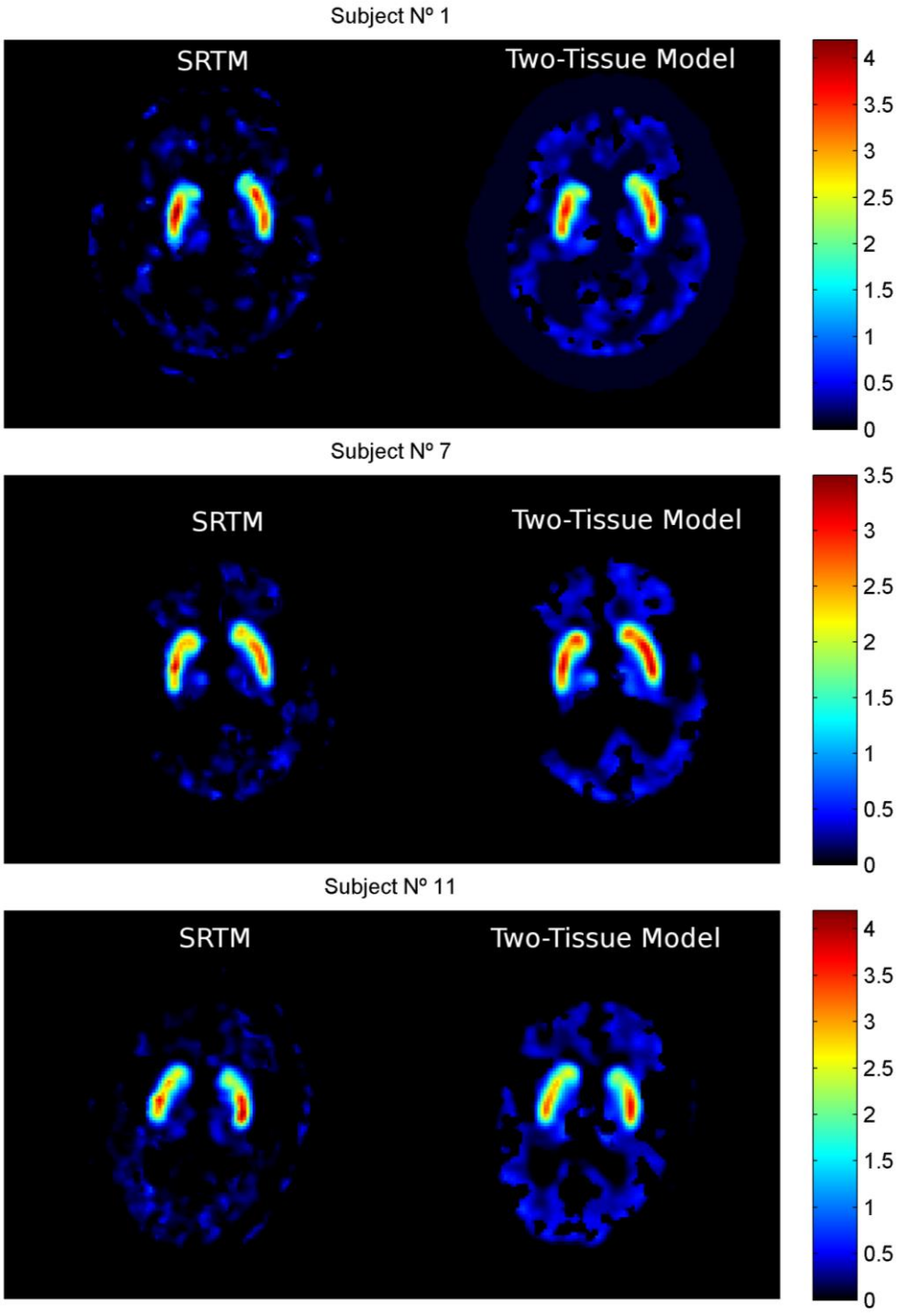

Figure 5.7 – Parametric images generated for 3 subjects. On the left, the parametric image generated using the SRTM and the reference region TAC as input. On the right, the parametric images generated using the two-tissue model and the IDIF as input. For all the subjects represented, the IDIF used was the one extracted with the HC method.

A correlation between each voxel from the parametric image determined with the SRTM and the corresponding voxel determined using the two-tissue model is

illustrated in Figure 5.8. For the three subjects, a good correlation between the BP values determined using the two different methods was found, with a slight tendency for the two tissue model to overestimate the BP, especially for low-binding zones, as is noticeable in figure 5.7.

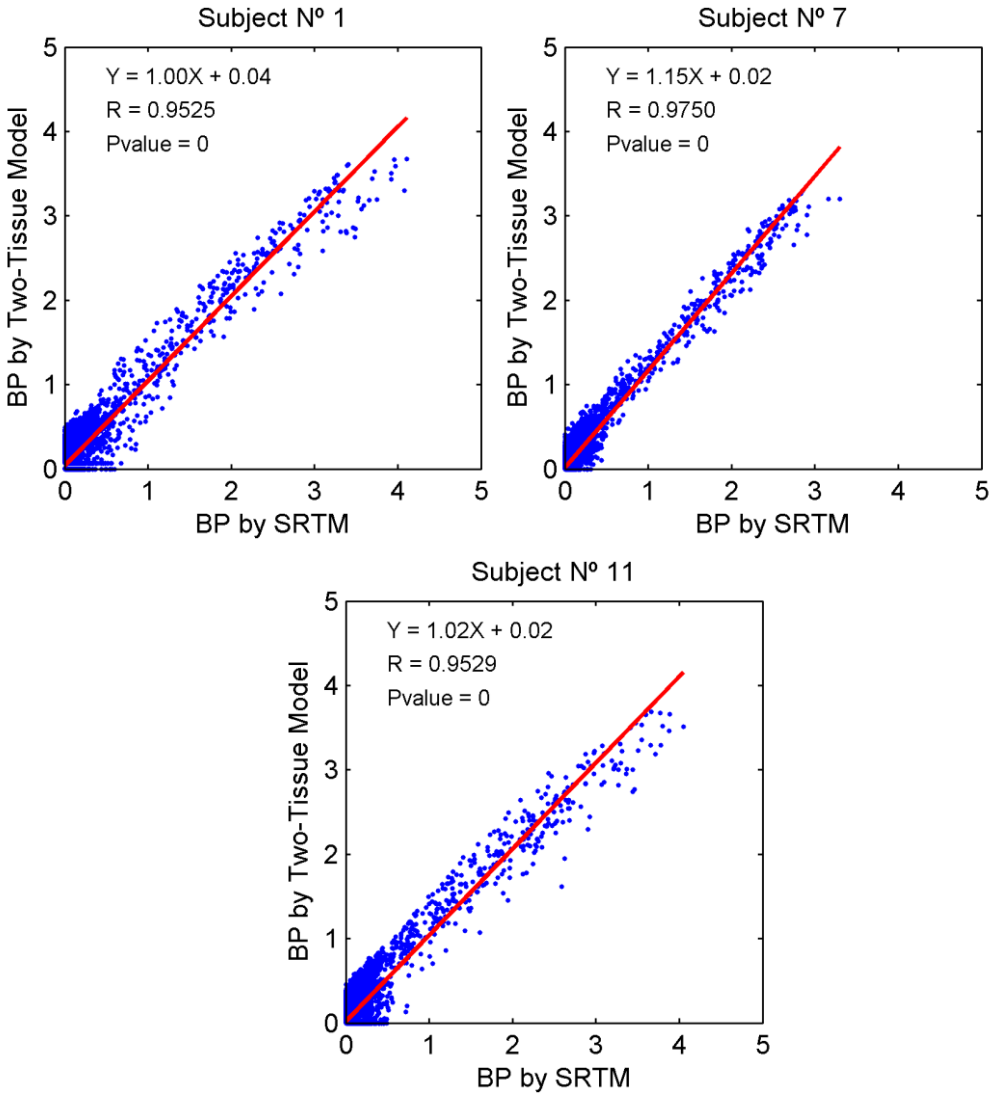

Figure 5.8 – Correlation between the voxel-wise BP values determined with the SRTM and the corresponding ones determined with the two-tissue model, for the parametric images of figure 5.7.

The best result achieved with the H4V method is represented in figure 5.9. It is possible to notice the overestimation of the binding potential, for both high-binding and low-binding zones.

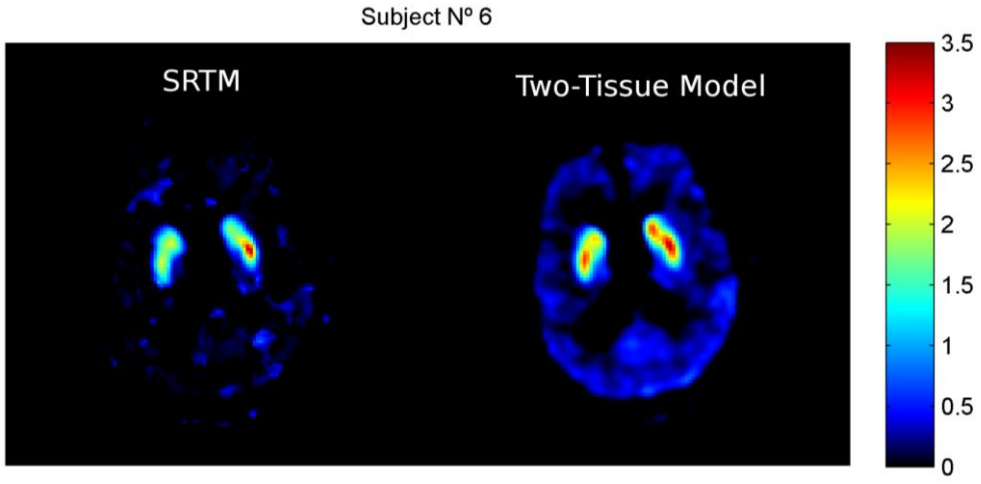

Figure 5.9 – Best result achieved in the generation of parametric images using IDIFs extracted with the H4V method.

The correlation of the result from the figure above shows a clear tendency for this method to overestimate the BP.

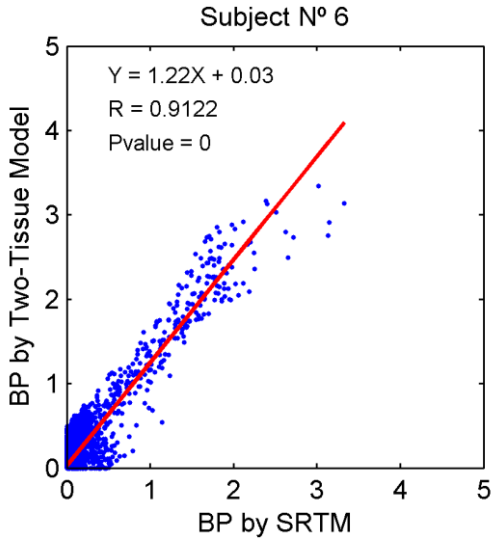

Figure 5.10 – Correlation between the voxel-wise BP values from the image determined with the SRTM and the corresponding ones from the image determined with the two-tissue model, referring to figure 5.9.

Unlikely using the two-tissue model, by generating the image quantification using the Logan Plot it was possible to quantify all images with good results, using both the IDIFs determined by the HC method and by the H4V method. This proves that the Logan plot is more robust with regard to IDIF errors in the calculation of the BP when compared to the two-tissue model. Table 5.3 shows the correlations between the voxels

from the parametric images generated with SRTM and the corresponding voxels from the parametric images generated with the Logan Plot, for both IDIF methods. Both methods achieved similar results, with high linear correlation coefficients and a tendency to underestimate the BP.

Table 5.3 – Correlation between the voxel-wise BP values determined with the SRTM and the corresponding ones determined with the Logan plot using both the IDIFs extracted with the HC method and the IDIFs extracted with the H4V method as input, for all subjects. All results were statistically significant.

Subject Nº	Hybrid Chen Method			Hottest 4 Voxels Method		
	Slope	Interception	R	Slope	Interception	R
1	0.94	0.01	0.98	0.78	-0.01	0.98
2	0.86	-0.01	0.98	0.86	-0.01	0.98
3	0.58	-0.01	0.94	0.83	0.00	0.97
4	0.81	0.00	0.94	0.79	0.00	0.89
5	0.74	-0.01	0.96	0.71	-0.01	0.96
6	0.84	-0.01	0.94	0.82	-0.01	0.98
7	0.92	0.00	0.99	0.91	0.00	0.99
8	0.95	0.00	0.98	0.95	0.00	0.99
9	0.82	-0.01	0.96	0.77	-0.01	0.96
10	0.79	-0.01	0.97	0.81	-0.01	0.97
11	0.87	0.00	0.98	0.87	0.00	0.98
12	0.76	-0.01	0.95	0.87	-0.01	0.97
13	0.89	-0.01	0.99	0.86	-0.01	0.98

Figure 5.11 illustrates the voxel-wise quantification of the same slices that had been included in figures 5.7 and 5.9, but this time the BP values were obtained using the Logan plot. On the left, the parametric image included was generated with SRTM. On the center, the parametric image was generated with the Logan plot using the IDIF extracted with the HC method. On the right, the image shown was generated with the Logan plot and the IDIF extracted with the H4V method.

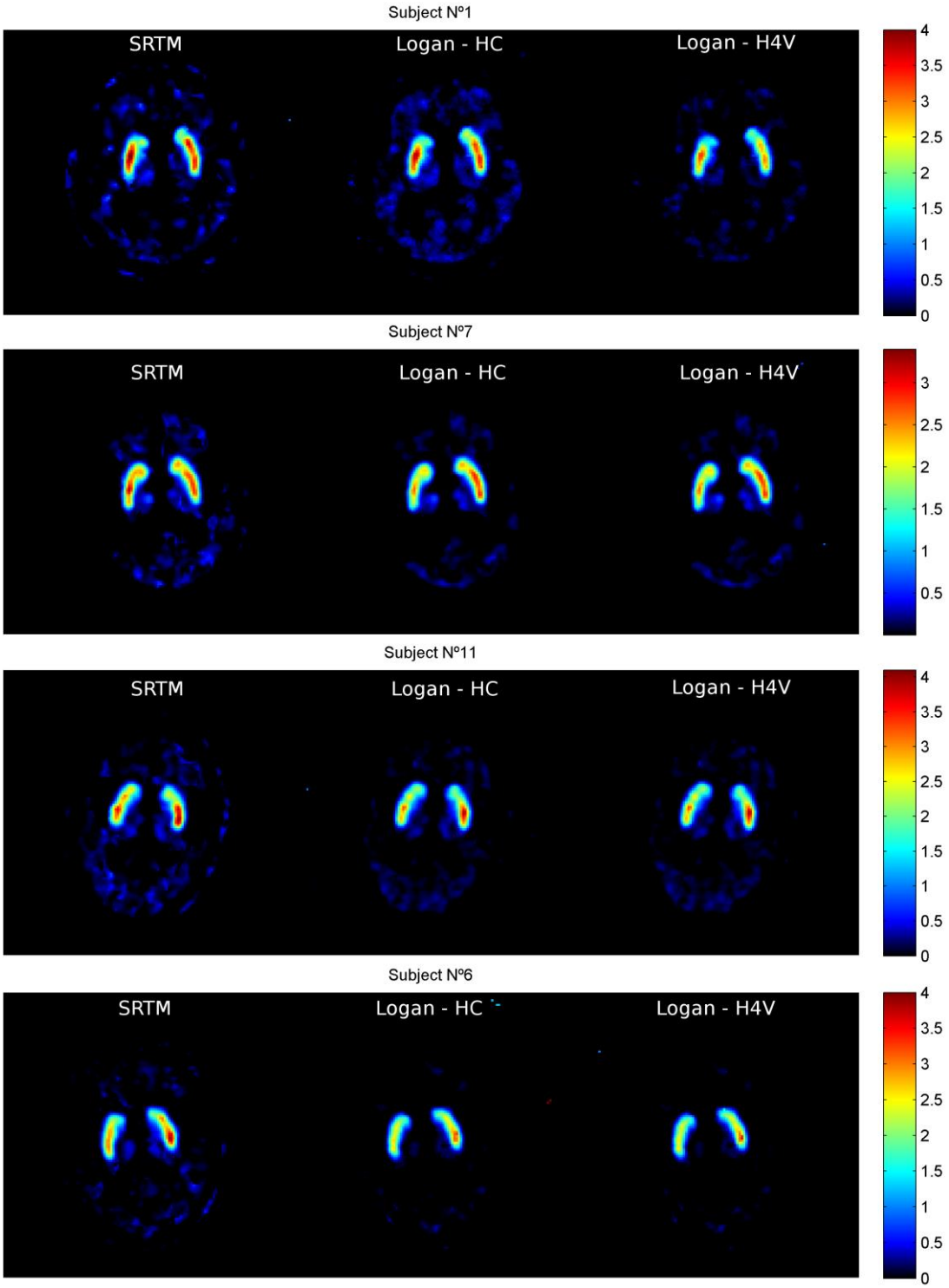

Figure 5.11 - Parametric images generated for the same subjects of figures 5.7 and 5.9, this time using the Logan plot. On the left, the parametric image generated using the SRTM and the reference region TAC as input. On the center, the parametric images generated using the Logan plot and the HC IDIFs as input. On the right, the parametric images generated using the Logan plot and the H4V IDIFs as input.

A correlation between each voxel from the parametric image determined with the SRTM and the corresponding voxel determined using the Logan plot, for subject number one, taking the IDIF obtained with the HC and H4V methods as input is represented in Figure 5.12. Similar results could be obtained for the other subjects.

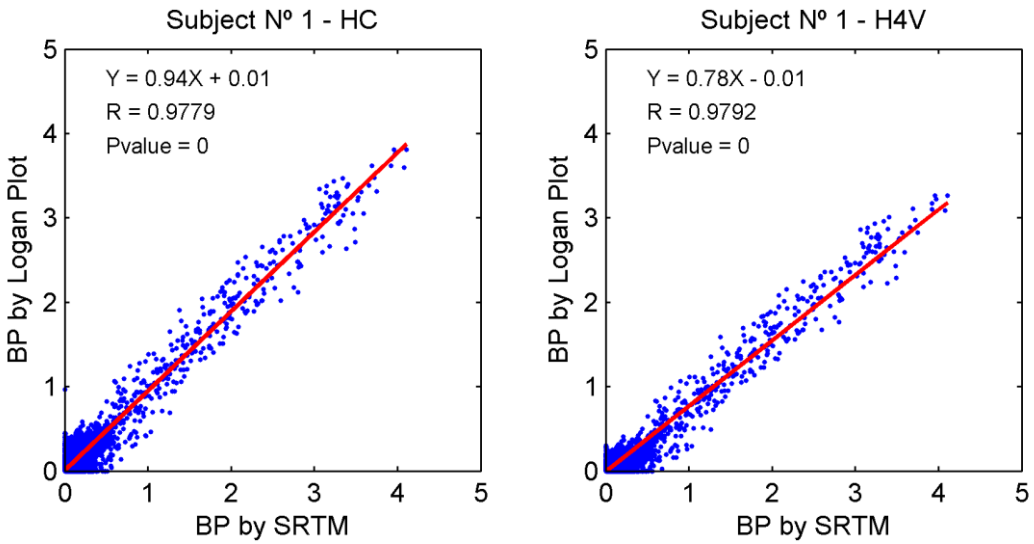

Figure 5.12 – Correlation between the voxel-wise BP values determined with the SRTM and the corresponding ones determined with the Logan plot, for subject nº1, using the IDIF extracted with the HC method (left) and the IDIF extracted with the H4V method (right) as input. This results are relative to the first sequence of images of figure 5.11.

5.5. Discussion

In this study, the two blood-free IDIF techniques evaluated in the chapter 4 were applied to [^{11}C]-Raclopride images. Binding potential quantifications were performed for each subject using the extracted IDIFs as input of the two-tissue compartmental model and of the Logan plot. The resulting BP estimates were compared to the BP determined using a validated alternative solution to the gold-standard method which requires arterial sampling: the SRTM, which uses as input a reference region (cerebellum) TAC.

The estimation of the BP from a striatum VOI for each subject, which is the target high-binding zone for [^{11}C]-Raclopride, provided the first evaluation of the IDIFs extracted with both the HC method and the H4V method.

In the first place, the two-tissue model lead to a considerable dispersion of the estimated BP values for the striatum VOI. That happened using the IDIFs of both the

HC method and of the H4V method. In addition, the BP values were in average overestimated in comparison to the BP values generated using the SRTM. The comparison between models mentioned in section 5.4.1, using perfect curves, expected an overestimation of the BP determined by the two-tissue model of about 6% when compared to the values determined with the SRTM. However even considering that assumption in the results, there was still a considerable overestimation of the BP. The HC method achieved the better performance by estimating BP with an average error of +16.55 ± 87.13%, while for the H4V the average error was +97.05 ± 165.34%. Recalling the results of the simulation performed in section 5.4.2, the overestimation of the binding potential had been associated to the underestimation of the peak and of the tail of the plasma curve, when the quantification was performed with the two-tissue model. The latter induces that probably the IDIFs estimated with both the HC method and H4V method were underestimated in comparison to the true AIF. Nevertheless, the HC method extracted IDIFs that, though still underestimated, were closer to the true input function values than the IDIFs extracted using the H4V method, since the average BP error of the latter was significantly higher. In fact, the H4V method produced for all subjects IDIFs with maximum peak values that were lower than the maximum peak values of the IDIFs extracted using the HC method, with an average relative difference of -14.4±11.23 %. The same happened for eleven of the thirteen subjects in the tail of the curves, with an average relative difference of -43.70±8.93%.

On the other hand, by using the Logan plot to determine the BP of the striatum VOI, a good accuracy was achieved using both IDIF methods. It had been found before, in section 5.4.2, that the Logan plot was robust to AIF errors in the estimation of the BP, since it relies on the ratio DV_{HIGH}/DV_{LOW}. In average, the BP values were slightly underestimated in comparison to the ones determined using the SRTM. It had also been found in section 5.4.2 that there was a tendency for the Logan plot to underestimate the BP when there was an underestimation of the tail of the AIF, see figure 5.3. In agreement with the conclusions derived from the two-tissue model, the underestimated BP results achieved with the Logan plot also suggest that there was an underestimation of the true AIF by the IDIF extraction methods. The estimated DV_{HIGH} and DV_{LOW} point to a bigger underestimation by the H4V method. According to figure 5.2 (b), the DV estimation by the Logan plot is particularly sensitive to errors in the tail of the input curve. Those results suggest that an overestimation of the DV is associated to an underestimation of the tail of the AIF. The IDIFs extracted with the H4V method

produced DV_{HIGH} estimates that were, on average, 54.18 ± 46.88% bigger than the DV_{HIGH} values estimated using the IDIFs from the HC method. This result is in agreement with the fact of the H4V method had produced IDIF tails that were lower-valued in comparison to the tails of the IDIFs extracted using the HC method, discussed in the previous paragraph.

The generation of parametric BP images, by individually quantifying each voxel, is more demanding, since the TAC of each voxel is more noisy than the averaged VOI TAC. Using the two-tissue compartmental model to obtain voxel-wise quantification, results close to the reference parametric maps were observed for three subjects. In all cases, the IDIFs had been obtained using the HC method. Since the two-tissue compartmental model has been shown to be considerably sensitive to AIF errors, see figures 5.1 (a) and 5.1 (b), it is very likely that the three IDIFs were good estimates of the true AIF. In general, the other quantified images revealed overestimation and dispersion of BP voxel estimates, from which reliable results were not obtainable. Similarly to the results obtained using the striatum VOI, the overestimation of the voxel-wise BP values are probably related to an underestimation of the true input function.

On the other hand, using the Logan plot, it was possible to quantify images for all the subjects, and high correlations between the SRTM quantified voxels and the voxels quantified with the Logan plot and IDIF were found. The slopes of the linear correlation equations revealed that in general, the BP of the voxels was slightly underestimated. As before, this underestimation of the BP is most likely related to the underestimation of the AIF by the blood-free IDIF methods.

Taken together, the comparisons of the BP values estimated by the validated alternative method SRTM and by the methods proposed in this study, in the context of the relations found with the simulation performed on the beginning of the chapter, suggest that probably a major source of error was an underestimation of the spill-out effects, leading to underestimated IDIF curves. Although relying on possibly noisy estimates of the true input function, the HC method achieved better results than the H4V method. In the first place, closer BP values were estimated for the striatum VOI using the two-tissue compartmental model. In the second place, three parametric images were good estimates. On the phantom study, also both methods produced underestimated peaks and tails, with slightly better results achieved with the HC method. As studied in the previous chapter, the possibility of the source of error being overestimation of the

tails, because of spill-in from the surrounding tissue in the late frames, was discarded since the tissue values were controlled and the carotid activity was superior for all subjects, in average by +28.31±12.38%.

It is also important to consider that several approximations were made. The parent fraction of radiotracer was not measured from blood samples; it was instead derived from the literature. Additionally, the plasma fraction was not measured, it was rather determined assuming a HCT value. And, most importantly, this was a totally non-invasive study that did not use blood samples to correct for PVE. In addition, it is important to mention that most studies that relied on the maximum carotid voxel values performed improvements in the reconstruction algorithm. Even with such improvements, reliable results are not always achieved. For example in the study (Jurgen E M Mourik et al. 2008), accurate IDIFs were obtained for [^{11}C]-Flumazenil relying on the four hottest voxels per plane, together with reconstruction improvements and blood samples used solely to correct the function for plasma fraction and metabolites. However when applying the same method to [^{18}F]-FDG, (Zanotti-Fregonara, Fadaili, et al. 2009) observed an underestimation of the of the AIF tail, in both phantoms and in clinical studies, which further lead to overestimated cerebral metabolic rate of glucose values.

5.6. Conclusion

In this chapter, the implementation of the blood-free IDIF methods studied in chapter 4 was made in [^{11}C]-Raclopride PET images to derive the AIF and determine the binding potential for a group of subjects.

The results suggest that relying on totally non-invasive IDIF methods for estimation of the AIF limits the possibility of obtaining good quantification estimates using the two-tissue compartmental model. The biggest obstacle seemed to be the underestimation of the spill-out effects, which could be improved by using some blood samples to calibrate the extracted TAC, according to the literature. Nevertheless, the HC method, although relying on a noisy approximation of the real concentration value, provided IDIFs which were closer to the real input function curves by providing a better estimation of the spill-out effects than the H4V method.

On the other hand, by performing the quantification using the Logan plot, good estimates of the BP were determined using both IDIF methods. However, although the

Logan plot method implemented uses the IDIF as the main input, it still relies on a reference region TAC to determine the DV of the reference region (DV_{LOW}). In the context of the problem that we are trying to solve this is not a valid solution, since the goal is to avoid the invasiveness of the gold-standard AIF estimation method, arterial sampling, for radiotracers in which a reference region is not available.

6. Summary and Conclusion

Deriving the AIF directly from the PET images by selecting the voxels corresponding to the internal carotid arteries and performing the related corrections is an attractive solution to the gold-standard method of arterial cannulation. Nevertheless, IDIF estimation has proven to be a technically challenging process. The low reproducibility of the methods across studies, due to the large number of factors that influence the reliability of IDIF estimation, has been an obstacle to the implementation of this technique in clinical protocols.

The biggest obstacle hindering the reliability of this technique are the PVE, in particular considering the carotid arteries diameter (5 millimeters) is close to the spatial resolution of PET cameras. The most successful IDIF techniques rely on using a number of blood samples to calibrate the function and correcting for PVE. In chapter 3, a study performed with a computational phantom allowed to understand the vulnerability of the blood-free methods to PVE and the gains to accuracy of using blood samples.

PVE have been a major issue since most studies in the literature relied on standard PET scanners with limited spatial resolution and high noise levels associated (Schain et al. 2013). Most recent PET scanners, as the HRRT, increased the resolution of the PET images and the success rate of IDIF estimation. Nevertheless, even in the most recent studies blood samples were still used for PVE corrections and other type of corrections, as determining the parent fraction of tracer and the plasma concentration, which also account for the reliability of IDIF estimation and must be determined for most tracers. In addition, a susceptibility to errors due to patient movements in the PET scanner has also been found in the literature. This type of error is particularly relevant for patients with neurologic conditions such as Parkinson's or Alzheimer's disease. Typically, the carotids are defined in the early frames, the ones in which they are more clearly identifiable. If throughout the scanning procedure there is significant movement by the patient, the delineated ROIs would not match the later frames, therefore causing IDIF errors (Zanotti-Fregonara & Liow 2012). (Mourik et al. 2011) showed that even a small amount of patient movement (5mm translation or 6 º rotations) was associated with large underestimation and overestimation in the final DV values. (Zanotti-

Fregonara & Liow 2012) observed that blood-based methods allowed accurate estimates of the DV even in cases of significant patient movements during the PET exam.

The current study was a proof-of-concept that IDIF can be estimated totally non-invasively and still provide good quantification estimates for [^{11}C]-Raclopride PET images in some cases, as seen in chapter 5. Nevertheless, good estimates were achieved for a limited number of subjects and results suggest that there was a tendency to underestimate the AIF due to PVE. It is also important to account that unlike the case of [^{11}C]-Raclopride, for most radiotracers the amount of metabolites produced substantially varies across subjects, and therefore the parent fraction curve has to be estimated individually.

All together, it seems that the IDIF technique, as a totally non-invasive alternative to the arterial cannulation, seems far from being reliable enough to be of widespread use. It is very dependent on the radiotracer used and on the image acquisition process. This is a technique that should be validated independently for each radiotracer and certainly for most of them blood sampling will be required. In the end, the IDIF has the advantage of reducing the number blood samples to draw and, depending on the radiotracer arteriovenous equilibrium time, using venous blood samples instead of arterial ones may be made possible.

The alternative solution to arterial cannulation, which is completely non-invasive, is using a reference region TAC as input of the reference tissue models. Nevertheless this is not always possible, since for many tracers or conditions a reference region is not available.

On the other hand, using a population-based input function (PBIF) is a potential good alternative. Although IDIFs are theoretically more flexible than the latter, because they calculate an individually tailored input function without assuming a common shape across different subjects, PBIF have the potential to reduce the number of blood samples used and is less time-consuming (Zanotti-Fregonara et al. 2012). However population based input functions have rarely been used to estimate the kinetic parameters with neuroreceptor PET studies.

In the future, when blood sampling is available, it will be possible to reliably use the methods assessed in this thesis on projects in IBILI/ICNAS, after the individual adaptation of the methods for each radiotracer. In particular, the usage of IDIF methods relying on venous blood samples will be a less invasive alternative to arterial cannulation when using reference region methods is not a possibility.

7. References

Bodvarsson, B. et al., 2006. Extraction of time activity curves from positron emission tomography: K-means clustering or non-negative matrix factorization. *NeuroImage*, 31, pp.p. T185–T186.

Bossong, M.G. et al., 2009. Delta 9-tetrahydrocannabinol induces dopamine release in the human striatum. *Neuropsychopharmacology : official publication of the American College of Neuropsychopharmacology*, 34(3), pp.759–66. Available at: http://www.ncbi.nlm.nih.gov/pubmed/18754005 [Accessed January 11, 2015].

Cai, W. et al., 2002. Generalized linear least squares algorithms for modeling glucose metabolism in the human brain with corrections for vascular effects. *Computer methods and programs in biomedicine*, 68, pp.1–14.

Chen, K. et al., 2007. Characterization of the image-derived carotid artery input function using independent component analysis for the quantitation of [18F] fluorodeoxyglucose positron emission tomography images. *Physics in medicine and biology*, 52(23), pp.7055–71. Available at: http://www.ncbi.nlm.nih.gov/pubmed/18029993.

Chen, K. et al., 1998. Noninvasive quantification of the cerebral metabolic rate for glucose using positron emission tomography, 18F-fluoro-2-deoxyglucose, the Patlak method, and an image-derived input function. *Journal of cerebral blood flow and metabolism : official journal of the International Society of Cerebral Blood Flow and Metabolism*, 18(7), pp.716–23. Available at: http://www.ncbi.nlm.nih.gov/pubmed/9663501.

Choi, Y. et al., 1991. Parametric images of myocardial metabolic rate of glucose generated from dynamic cardiac PET and 2-[18F]fluoro-2-deoxy-d-glucose studies. *Journal of nuclear medicine : official publication, Society of Nuclear Medicine*, 32, pp.733–738.

Croteau, E. et al., 2010. Image-derived input function in dynamic human PET/CT: methodology and validation with 11C-acetate and 18F-fluorothioheptadecanoic

acid in muscle and 18F-fluorodeoxyglucose in brain. *European journal of nuclear medicine and molecular imaging*, 37(8), pp.1539–50. Available at: http://www.pubmedcentral.nih.gov/articlerender.fcgi?artid=2914861&tool=pmcentrez&rendertype=abstract [Accessed April 8, 2014].

Delforge, J. et al., 1995. Quantification of benzodiazepine receptors in human brain using PET, [11C]flumazenil, and a single-experiment protocol. *Journal of cerebral blood flow and metabolism : official journal of the International Society of Cerebral Blood Flow and Metabolism*, 15, pp.284–300.

Everett, B. a et al., 2009. Safety of radial arterial catheterization in PET research subjects. *Journal of nuclear medicine : official publication, Society of Nuclear Medicine*, 50(10), p.1742. Available at: http://www.pubmedcentral.nih.gov/articlerender.fcgi?artid=3777228&tool=pmcentrez&rendertype=abstract [Accessed January 30, 2015].

Farde, L. & Halldin, C., 1989. Kinetic Analysis of Central [llC] Raclopride Binding to D2-Dopamine Receptors Studied by PET-A Comparison to the Equilibrium Analysis. , pp.696–708.

Feng, D., Huang, S. & Wang, X., 1993. Models for computer simulation studies of input functions for tracer kinetic modeling with positron emission tomography. *International journal of bio-medical …*, 32(1993). Available at: http://www.sciencedirect.com/science/article/pii/002071019390049C [Accessed December 14, 2014].

Fung, E.K. et al., 2009. A multimodal approach to image-derived input functions for brain PET. In *IEEE Nuclear Science Symposium Conference Record*. pp. 2710–2714.

Fung, E.K. & Carson, R.E., 2013. Cerebral blood flow with [15O]water PET studies using an image-derived input function and MR-defined carotid centerlines. *Physics in medicine and biology*, 58(6), pp.1903–23. Available at: http://www.pubmedcentral.nih.gov/articlerender.fcgi?artid=3626495&tool=pmcentrez&rendertype=abstract [Accessed April 8, 2014].

Gray, H., 1918. *Anatomy of the Human Body* 20th ed. W. Lewis, ed., Lea & Febiger. Available at: http://www.bartleby.com/107/146.html.

Gunn, R.N. et al., 1997. Parametric imaging of ligand-receptor binding in PET using a simplified reference region model. *NeuroImage*, 6(4), pp.279–287.

Herzog, H. et al., 2011. High resolution BrainPET combined with simultaneous MRI. *Nuklearmedizin. Nuclear medicine*, 50, pp.74–82.

Kropholler, M.A. et al., 2007. Evaluation of reference regions for (R)-[(11)C]PK11195 studies in Alzheimer's disease and mild cognitive impairment. *Journal of cerebral blood flow and metabolism : official journal of the International Society of Cerebral Blood Flow and Metabolism*, 27(12), pp.1965–1974.

Lammertsma, A. & Hume, S., 1996. Simplified reference tissue model for PET receptor studies. *Neuroimage*, 158(4), pp.153–158. Available at: http://www.sciencedirect.com/science/article/pii/S105381199690066X [Accessed November 5, 2014].

Lammertsma, A.A. et al., 1996. Comparison of Methods for Analysis of Clinical [llC] Raclopride Studies. , pp.42–52.

Leenders, K.L. et al., 1990. Cerebral blood flow, blood volume and oxygen utilization. Normal values and effect of age. *Brain*, 113, pp.27–47. Available at: http://www.ncbi.nlm.nih.gov/pubmed/2302536.

Liptrot, M. et al., 2004. Cluster analysis in kinetic modelling of the brain: A noninvasive alternative to arterial sampling. *NeuroImage*, 21(2), pp.483–493.

Litton, J.-E., 1997. Input Function in PET Brain Studies Using MR-Defined Arteries. , (4), pp.10–13.

Logan, J. et al., 1996. Distribution volume ratios without blood sampling from graphical analysis of PET data. *Journal of cerebral blood flow and metabolism : official journal of the International Society of Cerebral Blood Flow and Metabolism*, 16, pp.834–840.

Logan, J., 2000. Graphical analysis of PET data applied to reversible and irreversible tracers. *Nuclear Medicine and Biology*, 27(7), pp.661–670. Available at: http://linkinghub.elsevier.com/retrieve/pii/S0969805100001372.

Lüdemann, L. et al., 2006. Corrections of arterial input function for dynamic H215O PET to assess perfusion of pelvic tumours: arterial blood sampling versus image extraction. *Physics in medicine and biology*, 51, pp.2883–2900.

Mourik, J.E.M. et al., 2008. Image derived input functions for dynamic High Resolution Research Tomograph PET brain studies. *NeuroImage*, 43, pp.676–686.

Mourik, J.E.M. et al., 2011. Image derived input functions: Effects of motion on tracer kinetic analyses. *Molecular Imaging and Biology*, 13, pp.25–31.

Mourik, J.E.M. et al., 2008. Partial volume corrected image derived input functions for dynamic PET brain studies: methodology and validation for [11C]flumazenil. *NeuroImage*, 39(3), pp.1041–50. Available at: http://www.ncbi.nlm.nih.gov/pubmed/18042494 [Accessed March 25, 2014].

Naganawa, M. et al., 2005. Extraction of a plasma time-activity curve from dynamic brain PET images based on independent component analysis. *IEEE transactions on bio-medical engineering*, 52(2), pp.201–210.

Oikonen, V. et al., 2014. Turku PET Center - Converting blood TAC to plasma TAC. Available at: http://www.turkupetcentre.net/petanalysis/input_blood-to-plasma.html.

Oikonen, V., 2008. Turku PET Center - Hematocrit. Available at: http://www.turkupetcentre.net/petanalysis/hematocrit.html.

Parker, B.J. & Feng, D.F.D., 2005. Graph-based Mumford-Shah segmentation of dynamic PET with application to input function estimation. *IEEE Transactions on Nuclear Science*, 52(1), pp.79–89.

Patlak, C.S., Blasberg, R.G. & Fenstermacher, J.D., 1983. Graphical evaluation of blood-to-brain transfer constants from multiple-time uptake data. *Journal of*

cerebral blood flow and metabolism : official journal of the International Society of Cerebral Blood Flow and Metabolism, 3, pp.1–7.

Sanabria-Bohórquez, S., 2003. Image-Derived Input Function for [11C]Flumazenil Kinetic Analysis in Human Brain. *Molecular Imaging & Biology*, 5(2), pp.72–78. Available at: http://linkinghub.elsevier.com/retrieve/pii/S1536163203000465 [Accessed April 8, 2014].

Schain, M. et al., 2013. Arterial input function derived from pairwise correlations between PET-image voxels. *Journal of cerebral blood flow and metabolism : official journal of the International Society of Cerebral Blood Flow and Metabolism*, 33(7), pp.1058–65. Available at: http://www.ncbi.nlm.nih.gov/pubmed/23571279 [Accessed April 8, 2014].

Da Silva, N.A. et al., 2012. Image-derived input function obtained in a 3TMR-brainPET. *Nuclear Instruments and Methods in Physics Research, Section A: Accelerators, Spectrometers, Detectors and Associated Equipment*.

Silva, N.A.I.R. da, 2012. *On the Use of Image Derived Input Function for Quantitative PET Imaging with a Simultaneous Measuring MR-BrainPET*. University of Lisbon.

Su, K., Wu, L. & Liu, R., 2005. Quantification method in fluorodeoxyglucose brain positron emission tomography using independent component analysis. *Nuclear medicine …*, (2). Available at: http://journals.lww.com/nuclearmedicinecomm/Abstract/2005/11000/Quantification_method_in__18F_fluorodeoxyglucose.10.aspx [Accessed April 8, 2014].

Varga, J. & Szabo, Z., 2002. Modified regression model for the Logan plot. *Journal of cerebral blood flow and metabolism : official journal of the International Society of Cerebral Blood Flow and Metabolism*, 22, pp.240–244.

Watabe, H. et al., 2006. PET kinetic analysis--compartmental model. *Annals of nuclear medicine*, 20(9), pp.583–8. Available at: http://www.ncbi.nlm.nih.gov/pubmed/17294668.

Zanotti-Fregonara, P., Maroy, R., et al., 2009. Comparison of 3 methods of automated internal carotid segmentation in human brain PET studies: application to the estimation of arterial input function. *Journal of nuclear medicine : official publication, Society of Nuclear Medicine*, 50(3), pp.461–7. Available at: http://www.ncbi.nlm.nih.gov/pubmed/19223421 [Accessed April 1, 2014].

Zanotti-Fregonara, P., Fadaili, E.M., et al., 2009. Comparison of eight methods for the estimation of the image-derived input function in dynamic [(18)F]-FDG PET human brain studies. *Journal of cerebral blood flow and metabolism : official journal of the International Society of Cerebral Blood Flow and Metabolism*, 29(11), pp.1825–35. Available at: http://www.ncbi.nlm.nih.gov/pubmed/19584890 [Accessed April 8, 2014].

Zanotti-Fregonara, P. et al., 2011. Image-derived input function for brain PET studies: many challenges and few opportunities. *Journal of cerebral blood flow and metabolism : official journal of the International Society of Cerebral Blood Flow and Metabolism*, 31(10), pp.1986–1998. Available at: papers://2869f907-86c9-45b4-b3a1-9fd72ada1eca/Paper/p50324 [Accessed April 8, 2014].

Zanotti-Fregonara, P. et al., 2012. Minimally invasive input function for 2-18F-fluoro-A-85380 brain PET studies. *European journal of nuclear medicine and molecular imaging*, 39(4), pp.651–9. Available at: http://www.ncbi.nlm.nih.gov/pubmed/22231015 [Accessed April 8, 2014].

Zanotti-Fregonara, P. & Liow, J., 2012. Image-derived input function in PET brain studies: blood-based methods are resistant to motion artifacts. *Nuclear medicine …*, 33(9), pp.982–989. Available at: http://www.ncbi.nlm.nih.gov/pmc/articles/PMC3788705/ [Accessed April 8, 2014].

Zhou, S. et al., 2011. A method of generating image-derived input function in a quantitative ^{18}F-FDG PET study based on the shape of the input function curve. *Nuclear medicine communications*, 32(12), pp.1121–7. Available at: http://www.ncbi.nlm.nih.gov/pubmed/21946619 [Accessed April 8, 2014].